

AD-A085 874

CERAMIC FINISHING CO STATE COLLEGE PA

F/6 11/2

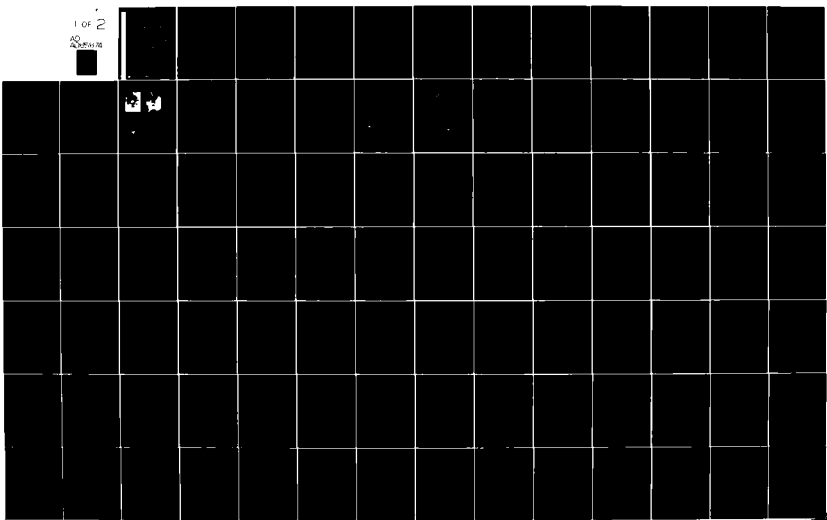
LOCALIZED IMPACT DAMAGE IN CERAMICS. LOCALIZED IMPACT DAMAGE TN--ETC(1)

FEB 80 H P KIRCHNER, T J LARCHUK, J M RAGOSTA N00014-74-C-0241

NL

UNCLASSIFIED

1 OF 2
2000-10



52
12
ADA 085874

Ceramic Finishing Company
State College, Pennsylvania 16801

TECHNICAL REPORT NO. 8

11
A 068 972

LOCALIZED IMPACT DAMAGE IN CERAMICS

Localized Impact Damage in Zinc Sulfide
Crack Growth from Small Flaws in Larger Grains in Alumina

February, 1980

Prepared by
H. P. Kirchner
T. J. Larchuk
J. M. Ragosta

JUN 24 1980

A

Prepared under Contract No. N00014-74-C-0241 for the
Office of Naval Research, Department of the Navy
Requisition No. NR032-545/12-17-73(471)

Distribution of this document is unlimited

80 6 23 004

DOC FILE COPY

SECURITY CLASSIFICATION OF THIS PAGE (When Data Entered)

REPORT DOCUMENTATION PAGE		READ INSTRUCTIONS BEFORE COMPLETING FORM
1. REPORT NUMBER	2. GOVT ACCESSION NO.	3. RECIPIENT'S CATALOG NUMBER
		4D-AC95 874
4. TITLE (and Subtitle)		5. TYPE OF REPORT & PERIOD COVERED
Localized Impact Damage in Ceramics		Technical Report Feb. 1, 1979-Jan. 31, 1980
6. PERFORMING ORG. REPORT NUMBER		
7. AUTHOR(S)		8. CONTRACT OR GRANT NUMBER(S)
H. P. Kirchner T. J. Larchuk J. M. Ragosta		15 N00014-74-C-0241
9. PERFORMING ORGANIZATION NAME AND ADDRESS		10. PROGRAM ELEMENT, PROJECT, TASK AREA & WORK UNIT NUMBERS
Ceramic Finishing Company P. O. Box 498 State College, Pennsylvania 16801		11
11. CONTROLLING OFFICE NAME AND ADDRESS		12. REPORT DATE
Office of Naval Research Department of the Navy Arlington, Virginia 22217		February 1980
14. MONITORING AGENCY NAME & ADDRESS (if different from Controlling Office)		13. NUMBER OF PAGES
11 Technical Rep. No. 8 1 Feb 79-31 Jan 80		98
16. DISTRIBUTION STATEMENT (of this Report)		15. SECURITY CLASS. (of this report)
Distribution of this document is unlimited.		Unclassified
17. DISTRIBUTION STATEMENT (of the abstract entered in Block 20, if different from Report)		15a. DECLASSIFICATION DOWNGRADING SCHEDULE
18. SUPPLEMENTARY NOTES		
19. KEY WORDS (Continue on reverse side if necessary and identify by block number)		
ceramics, zinc sulfide, alumina, localized impact damage, radial cracks, lateral cracks, median cracks, impact load, penetration of damage, subcritical crack growth, crack velocity, stress intensity factor, numerical integration		
20. ABSTRACT (Continue on reverse side if necessary and identify by block number)		
The following topics are covered in this report: (1) Localized impact damage in zinc sulfide. (2) Crack growth from small flaws in larger grains in alumina. Zinc sulfide specimens were damaged by static and impact loading using glass spheres. The various types of cracks were identified and their sizes were measured. The maximum impact loads were estimated by several methods including an experimental method based on the assumption that static and		

Impact loads are equal at equal indentation radii, a semi-empirical method previously developed on this program and a method suggested by Hutchings. The load (P) dependence of the crack length (c) for static and impact loading was best represented by

$$\frac{P}{d_i} \propto c^{\frac{1}{2}}$$

where d_i is the diameter of the indentation.

Crack growth in alumina was simulated for the case of small flaws in larger surface crystals to determine the range of crystal sizes and loading rates in which single crystal fracture energies would be expected to control fracture. This should be expected only for large crystals and very high loading rates.

Ceramic Finishing Company
State College, Pennsylvania 16801

TECHNICAL REPORT NO. 8

LOCALIZED IMPACT DAMAGE IN CERAMICS

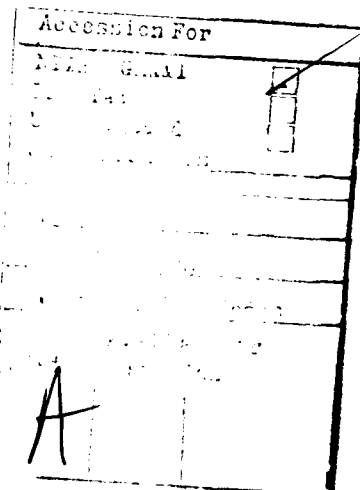
Localized Impact Damage in Zinc Sulfide

Crack Growth from Small Flaws in Larger Grains in Alumina

February, 1980

Prepared by

H. P. Kirchner
T. J. Larchuk
J. M. Ragosta



Prepared under Contract No. N00014-74-C-0241 for the
Office of Naval Research, Department of the Navy
Requisition No. NR032-545/12-17-73(471)

Distribution of this document is unlimited

TABLE OF CONTENTS

Report of Documentation Page	i
Title Page	iii
Forward	v
Localized Impact Damage in Zinc Sulfide	1
Crack Growth from Small Flaws in Larger Grains in Alumina	58
Basic Distribution List	92

FORWARD

This summary report describes research performed on a program sponsored by the Office of Naval Research, Department of the Navy, under contract N00014-74-C-0241. The research was performed under the general technical direction of Dr. Robert Pohanka, Metallurgy Branch of the Office of Naval Research.

The report covers work performed during the period of February 1, 1979 through January 31, 1980. The authors are pleased to acknowledge the contributions of their associates at Ceramic Finishing Company.

Localized Impact Damage

in Zinc Sulfide

by

H. P. Kirchner

T. J. Larchuk

**Ceramic Finishing Company
P. O. Box 498
State College, PA 16801**

ABSTRACT

Zinc sulfide specimens were damaged by static and impact loading using glass spheres. The various types of cracks were identified and their sizes were measured. The maximum impact loads were estimated by several methods including an experimental method based on the assumption that static and impact loads are equal at equal indentation radii, a semi-empirical method previously developed on this program and a method suggested by Hutchings. The load (P) dependence of the crack length (c) for static and impact loading was best represented by

$$\frac{P}{d_i} \propto c^{\frac{1}{2}}$$

where d_i is the diameter of the indentation.

I. INTRODUCTION

Several types of damage are induced when ceramic surfaces are contacted by small particles. These damage types include larger scale damage such as circumferential ring, Hertzian cone, median, radial and lateral cracks, and more localized damage such as plastic deformation, shear cracking and crushing, directly under the contact. Larger and blunter particles favor elastic responses such as circumferential and Hertzian cone cracks and crushing. Smaller and sharper particles favor elastic-plastic responses such as median, radial and lateral cracks, and plastic deformation at the impact site.

Much of what is known about the mechanisms of damage initiation and propagation has been learned by study of indentations formed under static loading (hardness) test conditions in which an indenter is pressed into a flat surface. Using small spherical tungsten carbide indenters and low loading rates, Evans and Wilshaw⁽¹⁾ observed the following sequence of crack formation in ZnS: (1) shallow radial surface cracks, (2) embedded penny-shaped cracks perpendicular to the surface (median vents), (3) merging of the median vents and radial cracks under coplanar conditions, and (4) subsurface cracks approximately parallel to the surface (lateral vents). Subsequently, Richard and Kirchner⁽²⁾ used results of static indentations and impacts of larger, 3 mm diameter, glass spheres on ZnS for a preliminary evaluation of a theory describing the elastic-plastic response to impact damage and Shockley, Dao and Curran⁽³⁾ investigated nucleation and growth of cracks at static indentations and impacts of small tungsten carbide spheres on ZnS.

Several mathematical models are available that can be used to predict

or scale the extent of damage due to static indentation or localized impact (Table I)⁽⁴⁻¹¹⁾. Use of these models depends on knowledge of the contact load. Direct measurement of the contact load is relatively easy for static indentations but, in the impact case, it is difficult at best.

In the present investigation, ZnS specimens were damaged by static and impact loading using glass spheres. The Young's modulus of glass is only about 70% as great as that of ZnS, so the glass is expected to be subject to substantial elastic deformation. On the other hand, the yield stress of ZnS is not very high compared with other ceramics, so an elastic-plastic response is expected. The contact damage was characterized. The impact loads were estimated using an experimental method based on the assumption that the static and impact loads are equal at equal indentation radii, and analytical methods using equations derived by Richard and Kirchner⁽²⁾ and Hutchings⁽¹²⁾. The variations in the extent of damage were scaled using selected models from Table I and the results were compared with experimental data.

TABLE I Crack Size Relations for Various Contact Conditions*

Contact	Material Response	Inden- ter Shape	Crack Type	$c = f(P)$	$P = f(c)$	Assumptions and Comments	References
Static- Central Loading	Elastic	Blunt	Hertzian Cone	$c \propto P^{2/3}$	$P \propto c^{3/2}$	c is diameter of cone at base $c \gg$ contact length	Lawn and Fuller(4) p. 2019
			Hertzian Cone	$c = \left(k(\nu) \frac{P}{K_{IC}} \right)^{2/3}$	$P = \frac{c^{3/2} K_{IC}}{k(\nu)}$	c is diameter of cone at base $c \gg$ contact length	Roesler(5) Lawn and Wilshaw(6)
Elastic- Plastic	Blunt	Radial		$c \propto \frac{P^{1/2}}{H^{1/4} K_{IC}^{1/3}}$	$P \propto c^2 H^{1/2} K_{IC}^{2/3}$	c is radial crack length, spherical indenter	Evans and Wilshaw(1) p. 22
		Lateral		$c \propto \left(\frac{P}{K_{IC}} \right)^{3/4}$	$P \propto c^{4/3} K_{IC}$	c is lateral crack length, spherical indenter	Evans and Wilshaw(1) p. 22
	Sharp	Radial		$c = \left(\frac{K_r P}{K_{IC}} \right)^{2/3}$	$P = \frac{c^{3/2} K_{IC}}{\chi_r}$	c is radial crack length	Marshall and Lawn(7) p. 2004
		Median		$c = \frac{\psi(\nu)}{K_{IC}} \left(\frac{a}{\beta^2} \right) H P$	$P = \frac{c K_{IC}}{\psi(\nu) H} \left(\frac{\beta^2}{a} \right)$	c is depth of median crack	Lawn and Wilshaw(6) p. 103
Impact- Central Loading	Elastic	Blunt	Hertzian Cone	$c \propto \frac{r_c E P}{Q r_o K_{IC}^2}$	$P \propto c \frac{Q r_o K_{IC}^2}{r_c E}$	c is length of cone crack measured along the slope	Evans(8)
Elastic- Plastic	Blunt	Radial		$c = \left(\frac{\chi_r}{K_{IC}} \right)^{2/3} V_o^{4/3} \left(\frac{\xi+2}{\xi+4} \right)$	—	$c = (\chi_r P / K_{IC})^{2/3}$ was assumed	Richard and Kirchner(2)

TABLE I continued

Contact	Material Response	Inden- ter Shape	Crack Type	$c = f(P)$	$P = f(c)$	Assumptions and Comments	References
		Median or Radial		$c \propto \left(\frac{P}{z_0}\right)^2$	$P \propto c^{1/2} z_0$	c is depth of median crack	Conway and Kirchner(9)
Line Loading	Elastic	Sharp	Wedge	$c = \left(\frac{K_L P}{L K_{IC}}\right)^2$	$P = \frac{c^{1/2} L K_{IC}}{\chi_L}$	c is depth of median crack	Lawn and Marshall(10)
Elastic- Plastic	Wedge	Median		$c = \frac{1}{\pi} \left(\frac{2.6 P_r}{K_{IC}}\right)^2$	$P_r = \frac{c^{1/2} \pi^{1/2} K_{IC}}{2.6}$	c is depth of median crack $c < \text{specimen depth}$ Loading due to residual stress	Tada, Faris and Irwin(11) p. 2-25

*See list of symbols on pages 47 and 48.

II. PROCEDURES

Zinc sulfide plates* (25 x 25 x 7 mm.) were indented by glass spheres**, 3 mm. diameter, under various loads using an Instron testing machine. Before testing, the plates were coated with a very light layer of soot. The contact boundary was marked by the impression left in the soot layer when the sphere was removed. The contact radii, indentation radii, numbers of radial cracks, and maximum radial and lateral crack lengths were measured using a calibrated eyepiece in an optical microscope, for a load range of 84 to 1059 N. Measurements of the maximum radial crack depth were made by viewing through the edge of the plates. Some test sites were too far from the edge to be measured.

Similar plates were impacted by glass spheres accelerated by a gas gun using compressed N_2 gas. The impact and rebounding velocities were measured using photographs with multiple stroboscopic images of the glass spheres. The spheres were coated with a thin layer of aluminum to improve their reflectivity. The impact velocity range was 19 to $65 \text{ m}\cdot\text{s}^{-1}$. The impact damage was characterized as described above for the static indentations. In some cases the profiles of the static and impact indentations were compared using a profilometer. The results were analyzed and are presented in the following section.

*Chemical vapor deposited zinc sulfide from Raytheon Company, Waltham, MA.

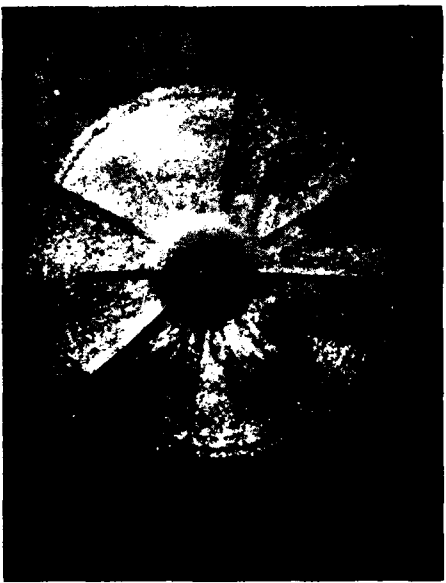
**No. 3000, Walter Stern Inc., Port Washington, NY.

III. RESULTS AND DISCUSSION

A. Comparisons of static and impact loading damage

The response of the ZnS plates to static and impact loading was elastic-plastic, yielding permanent indentations with the indentation radii increasing with load. The contact radii were slightly greater than the indentation radii, as expected. Ring cracks, radial cracks and lateral cracks were observed for both static and impact loading (Figure 1). Indentations were first observed at static loads of 40 N, but a load of at least 72 N was necessary to obtain a measurable indentation. At static indentations the load thresholds were 84 N for radial crack formation and 899 N for lateral crack formation. In the impact tests measurable indentations, radial cracking, and evidence of lateral cracking were observed at the lowest velocity tested, $19 \text{ m}\cdot\text{s}^{-1}$, and at all higher velocities.

Damage at static and impact sites was compared at approximately equal indentation radii as shown in Figure 1. When the indentation radii are relatively small, as in Figures 1 A (static) and 1 B (impact), the radial cracks formed at the impact sites are fewer in number and smaller than those formed at the static sites. However, in the impact case, lateral cracks initiate at smaller indentation radii as indicated by the lighter area to the left of the indentation. Also, the ring cracking is much more visible at the impact site. At larger indentation radii, as shown in Figure 1 C (static) and 1 D (impact), both the radial cracks and the lateral cracks are larger at the impact site than at the comparable static site. The lateral cracking at the impact site has produced chipping to the right of the indentation, while the static



A. Static Loading, $r_i \approx 260 \mu\text{m}$ (39X)



C. Static Loading, $r_i \approx 400 \mu\text{m}$ (19X)



B. Impact Loading, $r_i \approx 260 \mu\text{m}$ (39X)



D. Impact Loading, $r_i \approx 400 \mu\text{m}$ (19X)

Figure 1 Damage induced by static and impact loading (3 mm diameter glass spheres on ZnS plates).

site has no chipping. Also, the ring cracking within the impact indentations has become much more pronounced, causing the contour of the impact indentation to appear somewhat irregular, while the static indentation appears to be much smoother.

The irregularities observed in the impact indentations were investigated by profilometer measurements. Figure 2 shows the diametral profiles of static and impact indentations, compared at equal indentation radii. It should be noted that the vertical scale is ten times the horizontal scale. The distinguishing features are:

1. The impact indentations are much shallower than the static indentations.
2. The centers of the impact indentations are separated from the outer rims by substantial circumferential cracks, one of which is visible at the boundary of the dark central area in Figure 1 D.
3. The central areas of the impact indentations have been pushed down, apparently as a result of shear failures at the circumferential cracks.
4. The outer portions of the impact profiles form rims with much lower slopes than those of comparable static indentations.

The features described above indicate that, mechanically, the formation of impact indentations is much more complex than the formation of static indentations. These complexities are not presently understood. It is likely that some of these differences occur because of the strain rate dependence of the flow stress⁽¹³⁾. Because the flow stresses are higher during the early stages of impact when the strain rates are high,

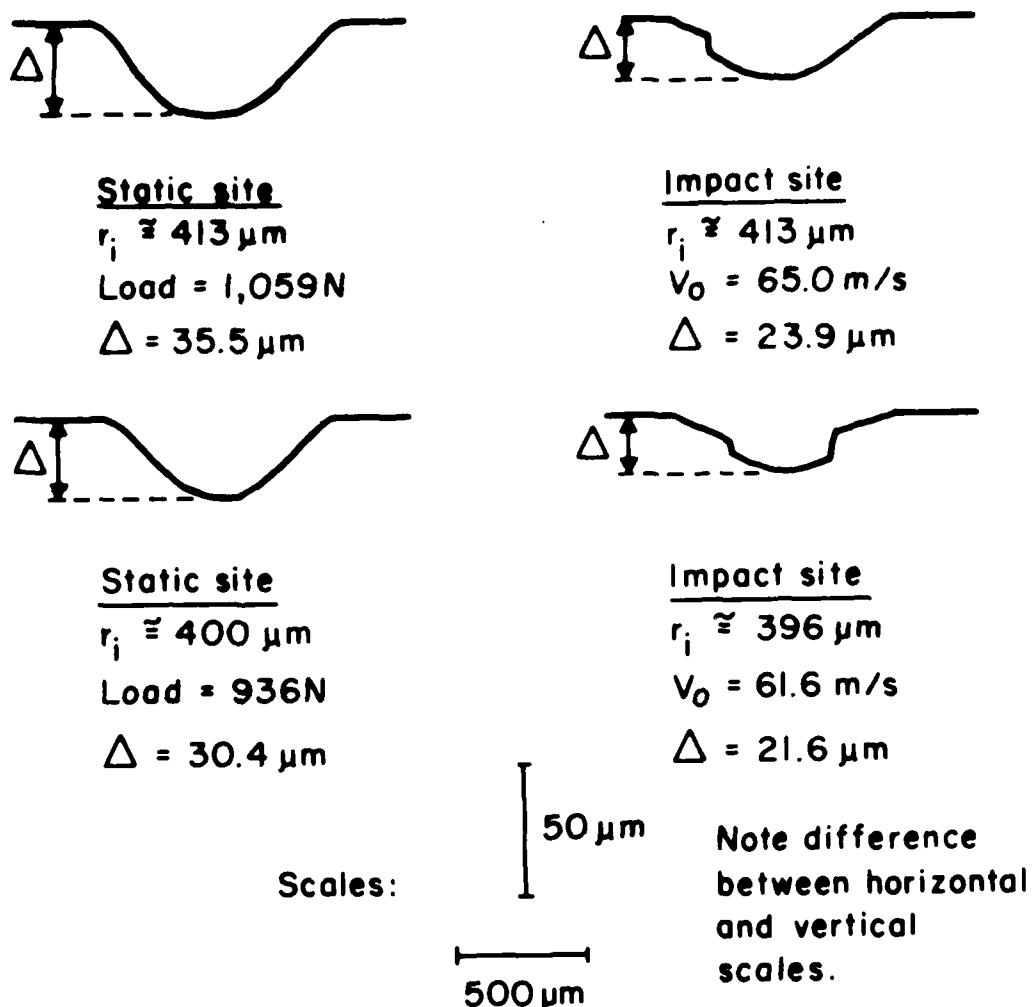


Figure 2 Diametral profilometer traces of static and impact indentations (ZnS, 3 mm diameter glass spheres).

the response is more elastic than it is in the static case. In metals, in which the yield stresses are a small fraction of Young's modulus, one might expect the response to be primarily plastic despite the increase in flow stress. However, in ceramics in which the yield stresses are usually a much larger fraction of Young's modulus, the response may be primarily elastic during the early part of the impact when strain rates are high. This may account for the reduced volume of the indentations and the smaller indentation depths in the impact specimens. Also, one would expect this greater resistance to deformation of the ZnS to be accompanied by greater elastic deformation of the glass spheres at each stage of the indentation.

One can speculate that the boundary formed by the wide circumferential crack represents a boundary between a central region in which forces tending to cause radial flow of the ZnS along the interface between the ZnS and glass are insufficient to overcome the frictional forces⁽¹⁾ and a circumferential band in which the frictional forces are overcome so that movement of ZnS radially along this interface does occur.

The existence of the deeper indentations at the static sites implies that the residual loads acting at these sites after the applied load is removed are larger than those at the impact sites. Such a difference in residual stresses may lead to observable differences in radial crack propagation⁽⁷⁾.

The sketches in Figure 3 present details of cracks observed by examining cross-sections of static and impact loaded specimens. The pairs of specimens have comparable indentation radii and are arranged in order of increasing indentation radius. The cross-section in Figure 3 A

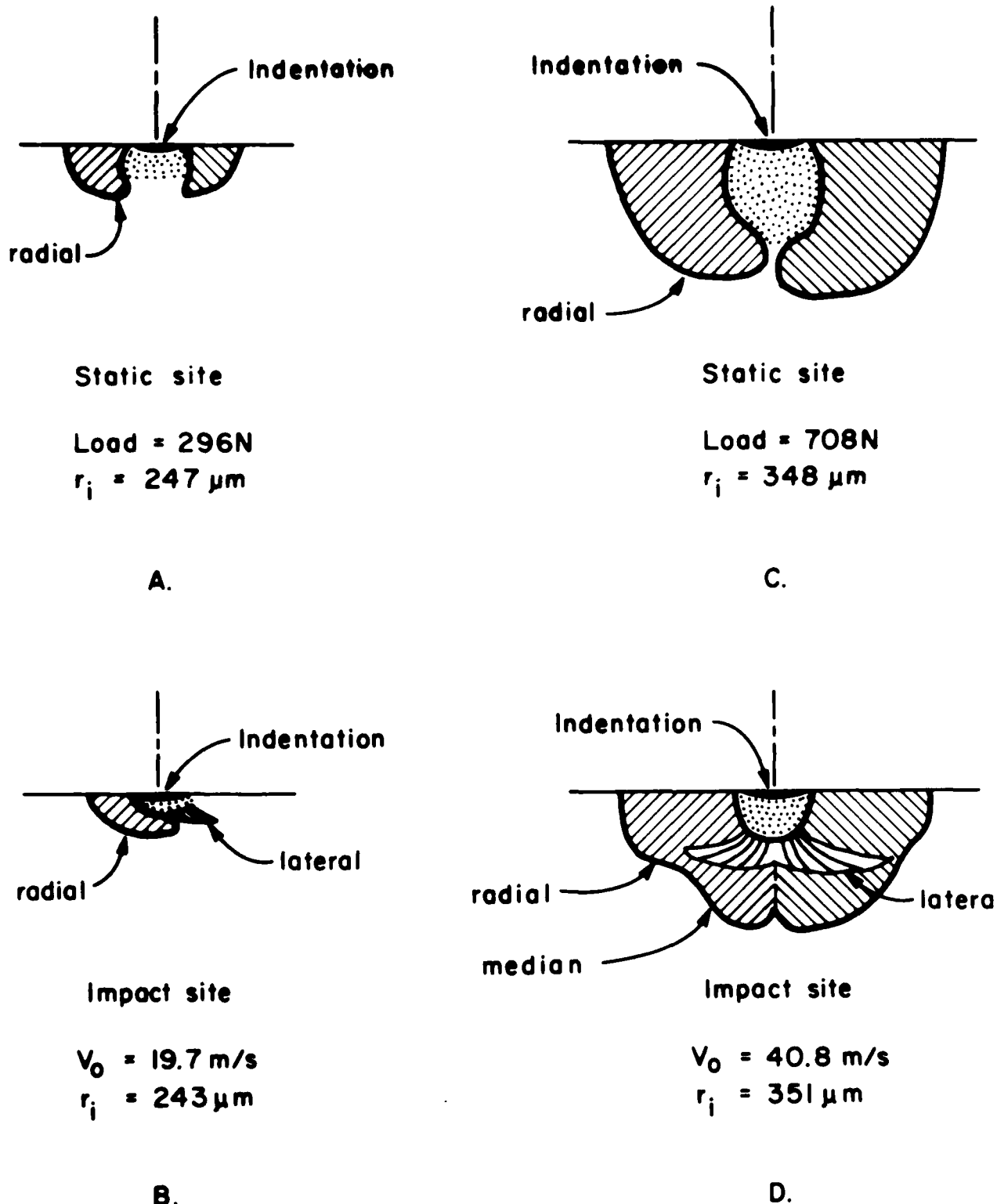
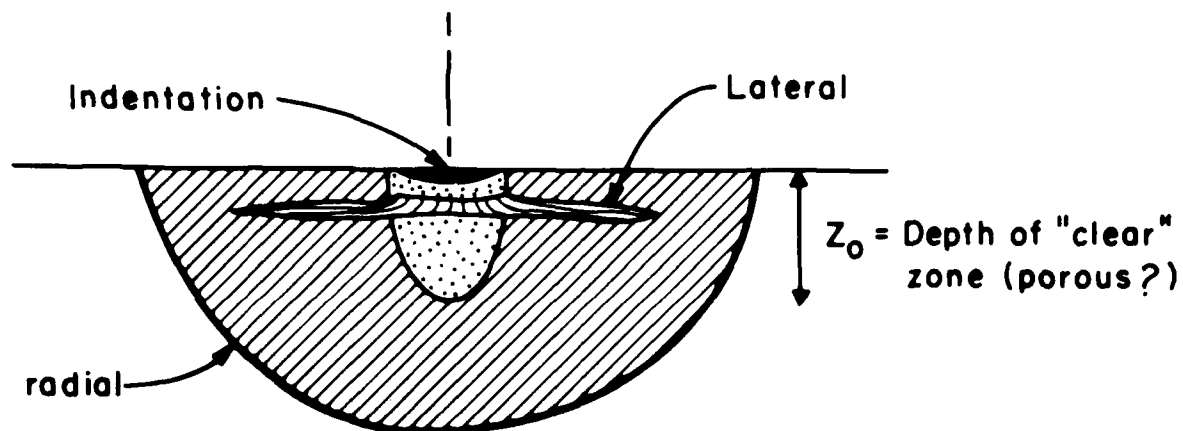


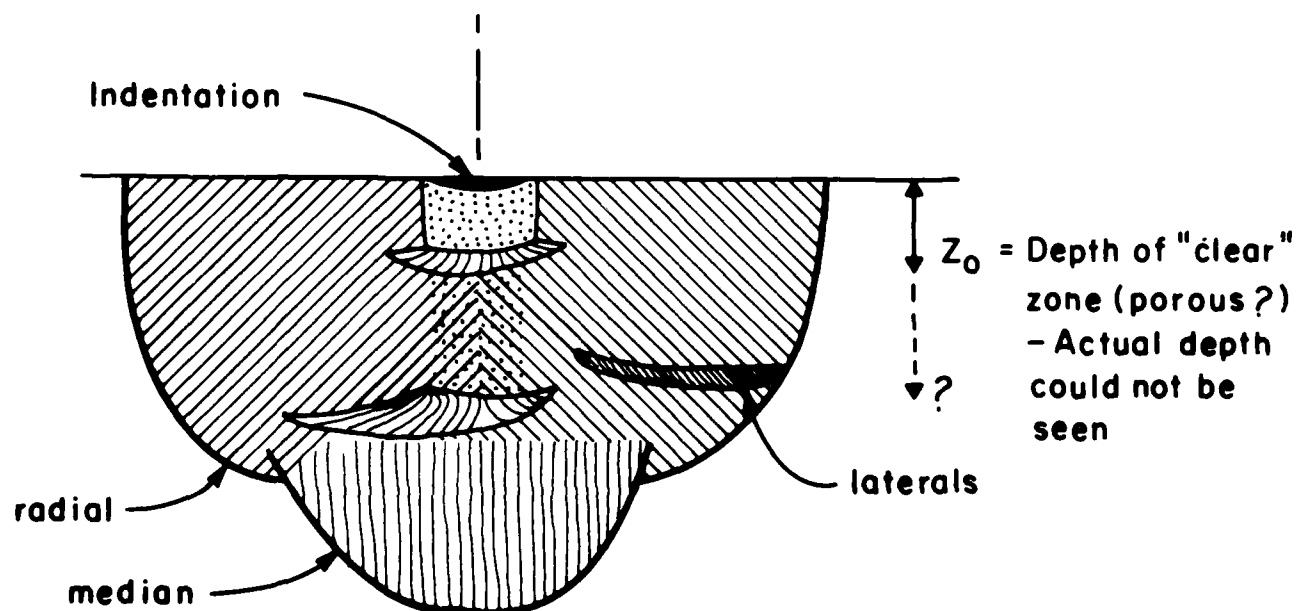
Figure 3 Comparisons of cracks formed at static and impact sites with comparable indentation radii (ZnS, 3 mm diameter glass spheres).



Static Site

Load = 936 N Δ = 30.4 μm
 r_i = 400 μm

E.



Impact site

V_0 = 61.6 m/s Δ = 21.6 μm
 r_i = 396 μm

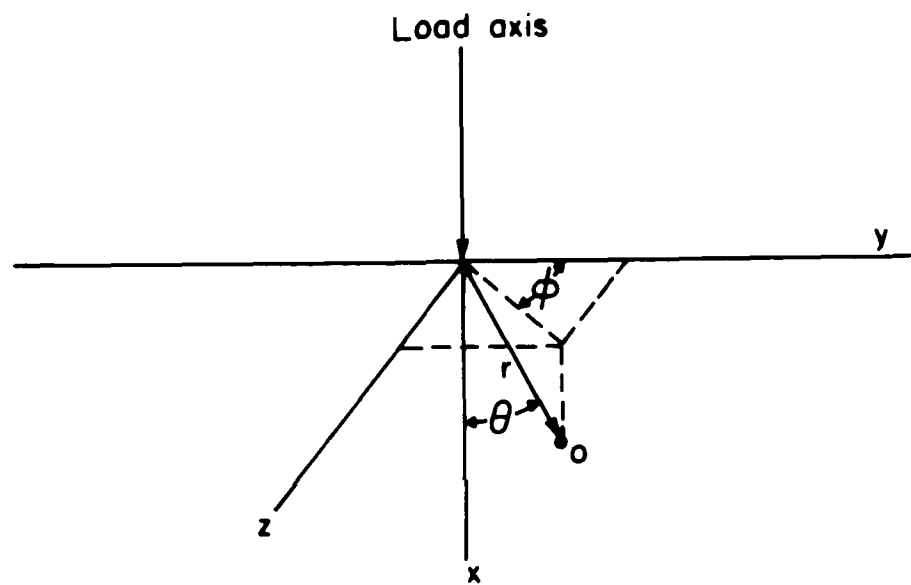
F.

represents damage at a small static indentation. The damage consists of radial cracks extending from the edges of the indentation and a slightly porous region under the indentation. The radial cracks are not necessarily coplanar and they do not bridge the gap under the indentation.

Evans and Wilshaw⁽¹⁾ observed that radial cracks form on loading. This observation is confirmed by observation of radial cracks that extend into the indentation (Figure 1 A). If the radial cracks formed on unloading, as a response to the residual stresses, the radial cracks would be expected to originate at the boundary of the irreversibly deformed zone.

Formation of radial cracks on loading implies that the out-of-plane hoop stresses (Figure 4) are tensile even when the indentations are very shallow. This condition conflicts with the conditions indicated for Boussinesq (point load at surface) and Hertzian (blunt load at surface) stress distributions⁽⁶⁾ and the results of calculations based on the Mitchell equations⁽⁹⁾ which indicate that the out-of-plane hoop stresses are compressive near the surface. For an extreme case in which a rigid sphere is pressed to the depth of its radius into the surface, numerical analyses of the elastic stress field by Evans and Wilshaw⁽¹⁾ have shown that the out-of-plane hoop stresses are tensile. If one considers that the irreversibly deformed zone acts in some ways like this embedded sphere to transfer the load into the interior of the specimen, it is understandable that the out-of-plane hoop stresses can be tensile even though the indentations are shallow. Friction may be another contributing factor.

The radial cracks initiate at the surface and spread outward along the surface but they do not spread downward into the material, appreciably, until they have grown out past the final indentation radius.



The surface of the plate is represented by the y - z plane. Due to symmetry, the reference plane is an arbitrary plane perpendicular to the y - z plane and containing the loading axis (x-axis). Then, at point O , σ_r is the radial stress, σ_θ is the in-plane hoop stress and σ_ϕ is the out-of-plane hoop stress.

Figure 4 Coordinate axes and identification of stresses.

The comparable impact site (Figure 3 B) has a somewhat similar radial crack on one side of the indentation and a small lateral crack on the other. The fact that, at small impact indentations, the radial cracks are smaller and less numerous is consistent with the earlier observation that the impact indentations are shallower, which would reduce the out-of-plane tensile stresses during loading and the residual stresses after unloading. The presence of the small lateral crack at the impact site and not at the comparable static site which is expected to have higher residual stresses, tends to refute the argument that the lateral cracks form in response to residual stresses. Instead, it is likely that this crack formed because the impact load is greater than the static load for a given indentation size so that the lateral crack formed in response to the greater in-plane hoop stress. The clear zone directly under the indentation is shallower in the impact case than it is in the static case. If this clear zone is considered to be a plastically deformed zone, perhaps formed in response to shear stresses, the decreased depth is consistent with higher flow stresses at higher strain rates. This observation is also consistent with Evans' observation that lateral cracking is more extensive in harder materials based on the increase in dynamic hardness with increasing strain rate.

At the next larger indentations (Figures 3 C, D), the radial cracks at the static indentation are much larger than those in Figure 3 A, and they have extended under the indentation so that they almost close the gap. Otherwise, the damage is similar to that in Figure 1 A. The impact damage shows larger radial and lateral cracks, as expected. In addition, under the clear zone, there are cracks extending deeper into the ZnS perpendicular to the surface that have been labelled as median

cracks. These cracks are not coplanar and the vertical line extending along the impact axis represents the intersection of the cracks. Median cracks are frequently observed at static indentations under sharp indentors. As the load is removed, radial cracks may extend in response to residual stresses and merge with existing median cracks. Apparently, this has occurred in the present case.

At the largest indentations (Figure 3 E, F), the radial cracks at the static indentation are even larger and they have extended under the indentation to completely close the gap to form an approximately semi-circular crack. A large lateral crack was observed close to the surface. The impact damage shows larger non-coplanar radial cracks and larger lateral cracks compared with those in Figure 3 D. Again, the median cracks have merged with the radial cracks. Lateral cracks are observed at several levels, all farther from the surface than the lateral crack at the comparable static site.

The numbers and lengths of cracks in static and impact loaded specimens are compared in Figures 5 and 6. Radial cracks are observed at smaller indentation radii at static indentations, and larger numbers of radial cracks are formed at a given indentation radius (Figure 5). The number of radial cracks depends on the total tensile strain at the periphery of the indentation. Therefore, observation of larger numbers of cracks at static indentations indicates more total tensile strain in these cases. Apparently, the high flow stress at high strain rates reduces the total strain in the impact cases.

Radial cracks at static indentations are longer than those at impact sites for indentation radii up to about $400 \mu\text{m}$ (Figure 6). At greater radii the radial cracks at impact sites are longer. If the

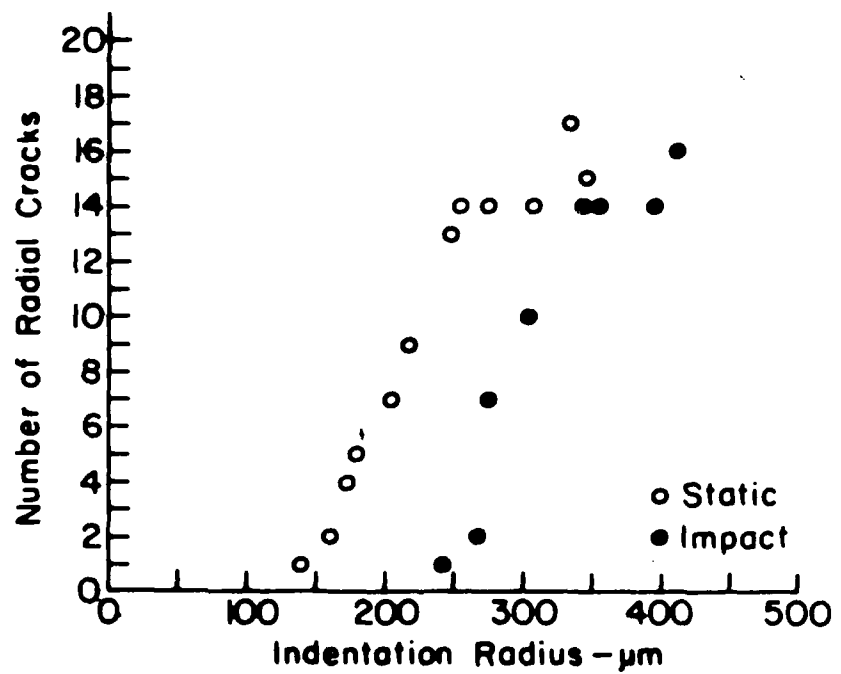


Figure 5 Number of radial cracks vs. indentation radius for static and impact loading (ZnS, 3 mm diameter glass spheres).

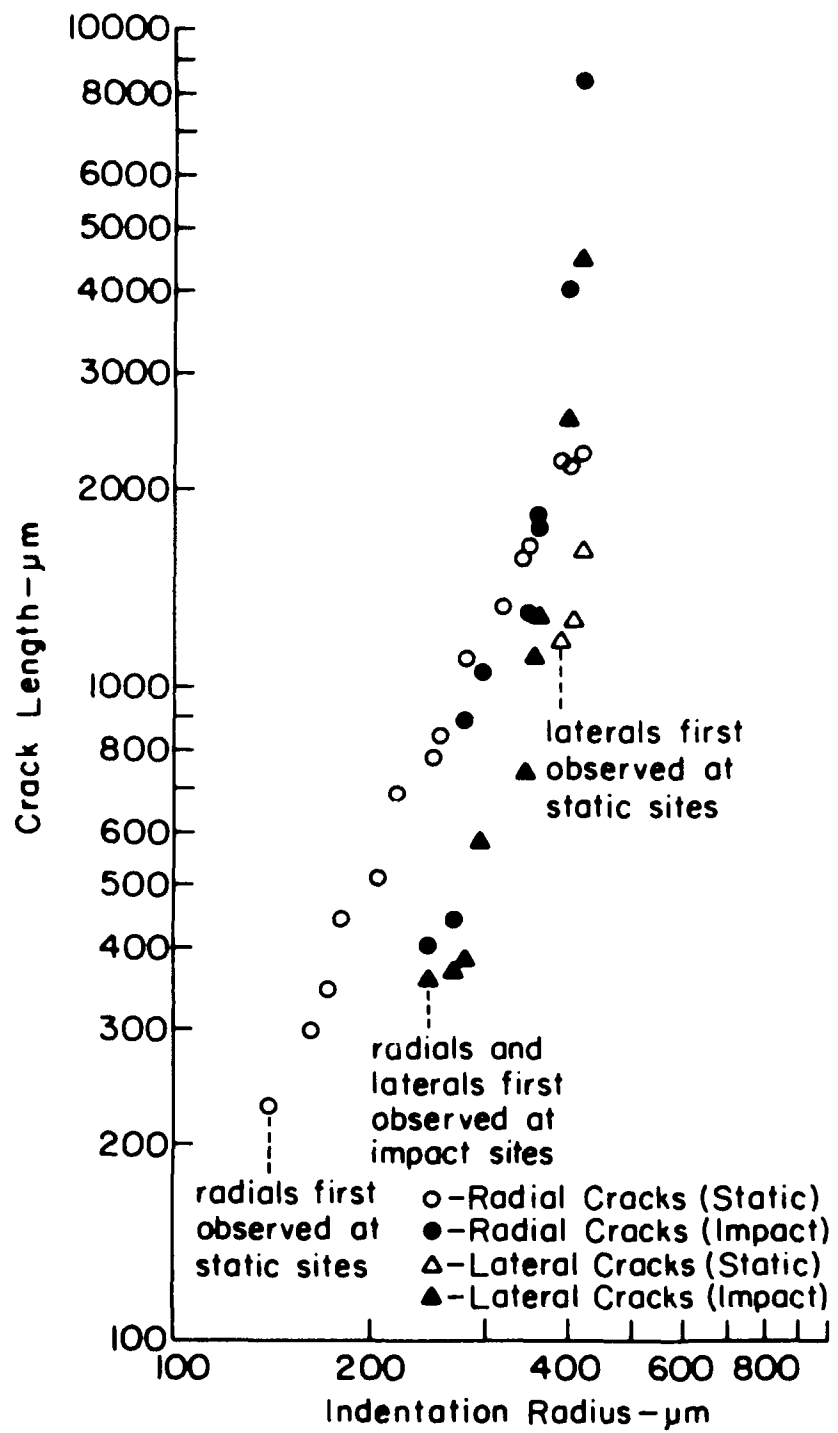


Figure 6 Crack lengths for static and impact radial and lateral cracks vs. indentation radius (ZnS, 3 mm diameter glass spheres).

arguments presented previously are correct, the lengths of the radial cracks depend on the loads and the depths of the irreversibly deformed zones which, in turn, influence the magnitude and size of the out-of-plane hoop stresses and the residual stresses. Apparently, at small indentation radii, the deeper indentations and greater plastic deformation observed in the static sites (leading to greater residual stresses) result in greater out-of-plane hoop stresses than those present at comparable impact indentations. However, at large indentation radii, the larger loads necessary to overcome the high flow stresses at high strain rates become dominant and the cracks are larger than those at static indentations.

B. Impact loads

To estimate the crack lengths using the equations in Table I, it is necessary to estimate the maximum impact loads. Five methods of estimating these loads are described in Table II.

To determine the impact loads by the first method, the load(P) vs. indentation radius (r_i) data from the static indentation tests were plotted (Figure 7). The data were fitted by a power law equation using the least squares method yielding

$$r_i = 2.10 \cdot 10^{-5} P^{0.43} \quad (1)$$

The fact that the exponent of P is less than 0.5 indicates that P is increasing faster than the area of the indentation. In other words, strain hardening is occurring. Similarly, the impact velocity (v_o) vs. indentation radius data from the impact tests are presented in Figure 8.

TABLE II Contact Load Equations

Equation	Source	Type of Material Response	Assumptions and Comments
$P = 13.25 V_o^{1.05}$	This investigation	Elastic-plastic	Equal r_i at equal static and impact loads
$\frac{2(\xi+2)}{\xi+4}$	Richard and Kirchner (2)	Elastic-Plastic	Equal impact and static loads produce equal contact radii; ξ and κ are statically determined parameters which account for the effects of work hardening and sphere size.
$\Omega = \kappa \pi r_o^2 \frac{M(\xi+4)}{24\pi r_o^3}$	in which $\frac{\xi+2}{\xi+4}$		
$P = \frac{4}{3} \pi r_o^2 \rho_1 V_o (3\rho_d/2\rho_1)^{\frac{1}{2}}$	Hutchings (12)	Plastic	η_H = impact pressure, assumed to be constant.
$P = \left(\frac{n+2}{4}\right)_A \frac{W_{pl.}}{Vol.}$	Tabor (15)	Elastic-plastic	P/A = impact pressure (dynamic hardness) = constant; $Vol.$ = the volume of the indentation; $W_{pl.}$ = energy of plastic deformation; $p_{npl.} =$ Meyer's index; $\left(\frac{n+2}{4}\right)$ accounts for work hardening.
$P = A^5 \left(\frac{1280}{243\pi^4}\right) \rho_1 V_o^2 \left(\frac{1}{f(E)}\right)^4$	Hutchings (14) (based on Hertz theory)	Elastic	P/A = maximum mean contact pressure $f(E) = \frac{1-\nu_1}{E_1} + \frac{1-\nu_2}{E_2}$

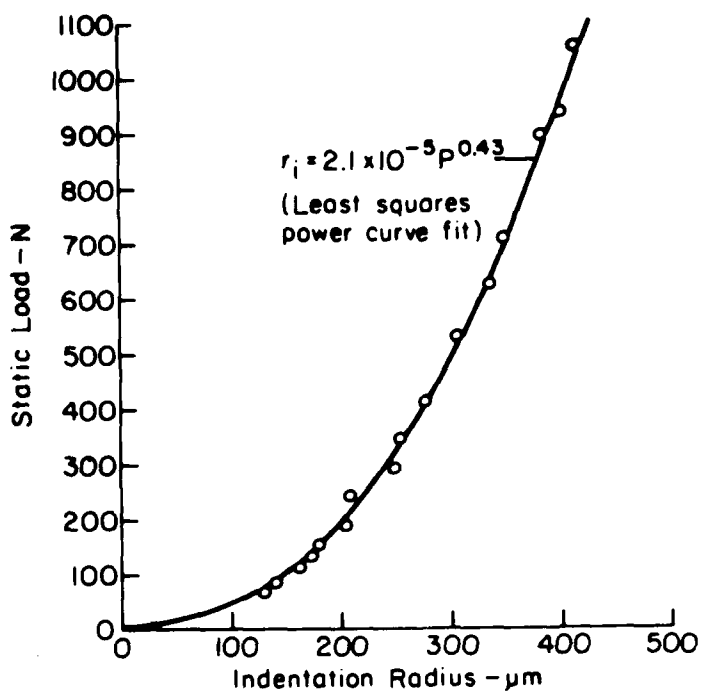


Figure 7 Static load vs. indentation radius (ZnS, 3 mm diameter glass spheres).

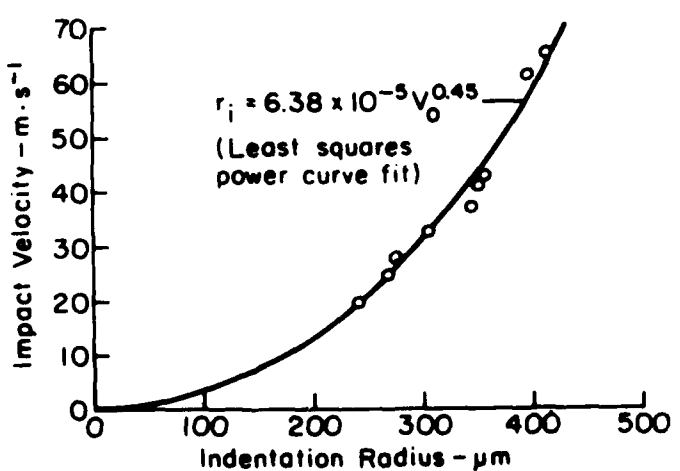


Figure 8 Impact velocity vs. indentation radius (ZnS, 3 mm diameter glass spheres).

The data were fitted yielding

$$r_i = 6.38 \cdot 10^{-5} v^{0.45} \quad (2)$$

Equations (1) and (2) were combined to obtain the impact velocity dependence of the load which was

$$P = 13.25 v_o^{1.05} \quad (3)$$

assuming that the static and impact loads are equal at equal indentation radii (Figure 9). This calculated load increases slightly faster than the velocity. In the elastic case (the Hertz theory), the theoretical value of the exponent is 1.2. For the perfectly plastic case, Hutchings⁽¹²⁾ found that the maximum load was proportional to the impact velocity. It is reasonable that the above results fall between these ideal cases.

It should be pointed out that this method fails to account for inertial effects and the increase in flow stress with strain rate. Both of these effects would be expected to increase the maximum impact load over that calculated, using this method. However, the method does account for strain hardening to the extent that it has increased the static indentation loads.

Richard and Kirchner method

Richard and Kirchner⁽²⁾ described a semi-empirical method of determining the load in impact experiments. This method is based on the empirical relations

$$\eta = \kappa \left(\frac{r_c}{r_o} \right)^\xi \quad (4)$$

$$\text{and} \quad \eta' = \kappa' \left(\frac{r_i}{r_o} \right) ^{\xi'} \quad (5)$$

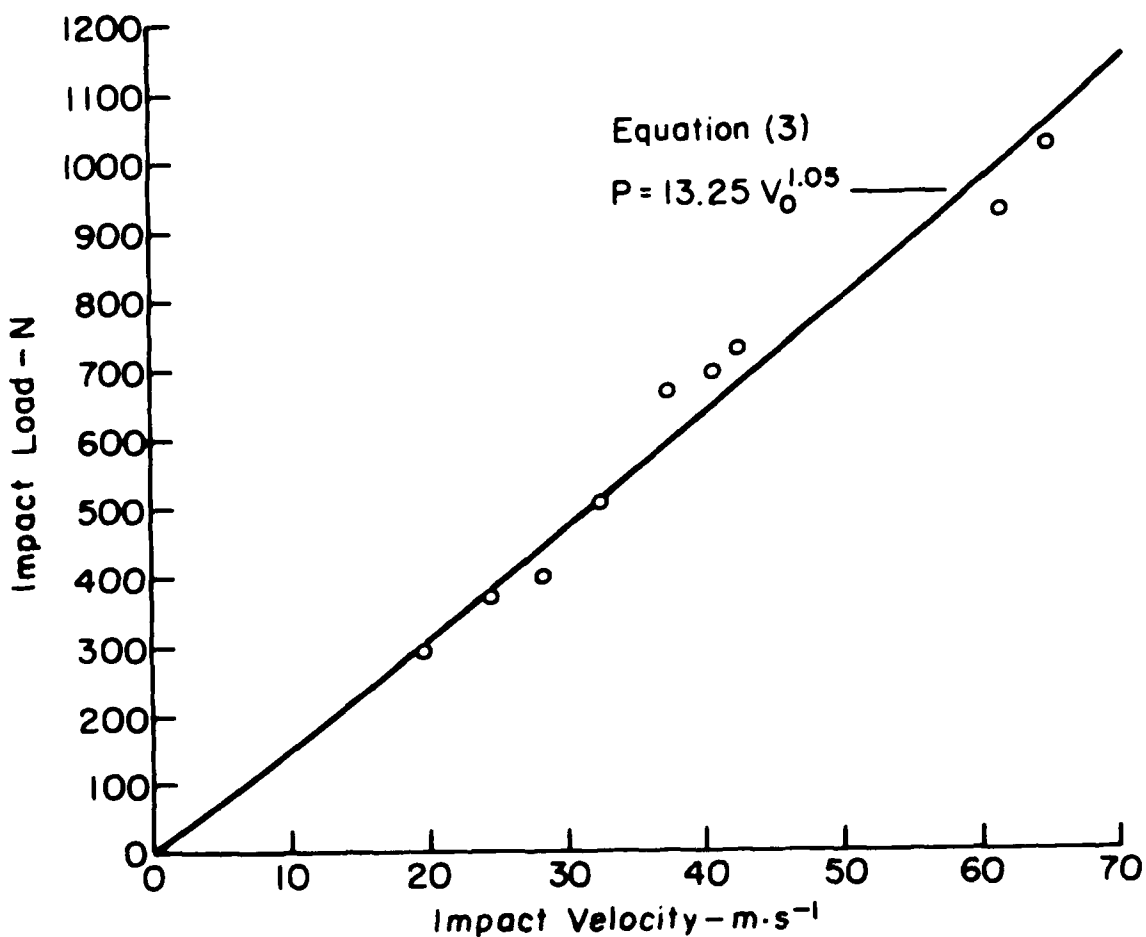


Figure 9 Impact load vs. impact velocity (The data points were determined by substituting impact r_i values in equation (1) to calculate impact load which was plotted vs. experimental impact velocity; ZnS, 3 mm diameter glass spheres.).

in which $\bar{\eta}$ and $\bar{\eta}'$ are the pressures averaged over the projection of the combined contact and indentation areas and the indentation areas respectively, r_c is the contact radius, r_i is the indentation radius, r_o is the sphere radius and κ , κ' , ξ and ξ' are empirical constants to be determined experimentally. Figure 10 shows that the logarithmic indentation relationship is approximately linear and that representation of the data by the above equations is reasonable. Also, these results can be compared with those of Evans and Wilshaw⁽¹⁾ for smaller spheres. The contact parameters were determined from the slopes and intercepts of plots of this type with the results shown in Table III and compared with similar results of Richard and Kirchner⁽²⁾. The rather large difference in the value of κ' between the two investigations apparently arose as a result of differences in criteria for locating the indentation boundaries adopted by the person making the measurement in each case.

TABLE III Contact Parameters

	ξ'	κ' GNm ⁻²	ξ	κ GNm ⁻²
Present investigation	0.34	3.0	0.71	4.9
Richard and Kirchner ⁽¹⁷⁾	0.27	5.5	0.78	5.5

The load is calculated by substituting the contact parameters κ and ξ , determined from static indentations in

$$P = \Omega V_o^2 \frac{(\xi+2)}{\xi+4} \quad (6)$$

$$\text{where } \Omega = \kappa \pi r_o^2 \left[\frac{M(\xi+4)}{2 \kappa \pi r_o^3} \right]^{\frac{\xi+2}{\xi+4}}$$

and used to calculate the impact load. Unlike equation (3), this

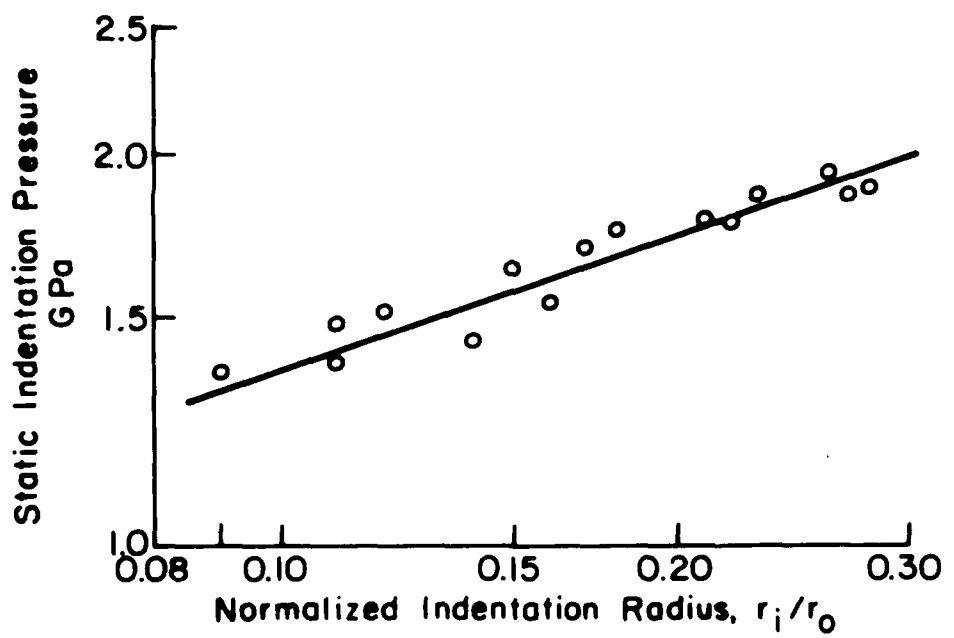


Figure 10 Static indentation pressure vs. the normalized indentation radius, r_i/r_o (ZnS statically loaded by 3 mm diameter glass spheres).

method accounts for the increases in pressure caused by inertial effects. However, it does not account for the increase in load caused by other material related factors that may contribute to the strain rate dependence of the flow stress or the decrease in load caused by the stress wave energy loss.

The third method that was used is Hutchings method⁽¹²⁾ which is described in Appendix A and compared with the first two methods. The remaining methods listed in Table II were not investigated.

The loads calculated using the first two methods are plotted in Figure 11, showing that there are substantial differences in the calculated load depending on the particular method used for the calculation. It seems likely that the loads obtained using equation (3) are underestimated because the inertial effects and the strain rate dependence of the flow stress are not accounted for. The loads obtained using equation (6) may be overestimated or underestimated. The fact that the contact radii are overestimated, (Figure 12) using the theory of Richard and Kirchner (the contact radii were calculated using equation (6) of reference (2)), indicates that equation (6) might tend to overestimate the loads, but the neglect of the strain rate dependence of the flow stress by equation (6) would tend to underestimate them. In fact, the lower contact radii observed experimentally may occur partly because of this strain rate dependence of the flow stress and partly because of the stress wave energy loss.

In evaluating the strain rate dependence of the flow stress, it is well to remember that the strain rate varies with time during the loading cycle. Initially, the strain rate is high because the velocity is high but, as the sphere slows down, the strain rate will decrease so

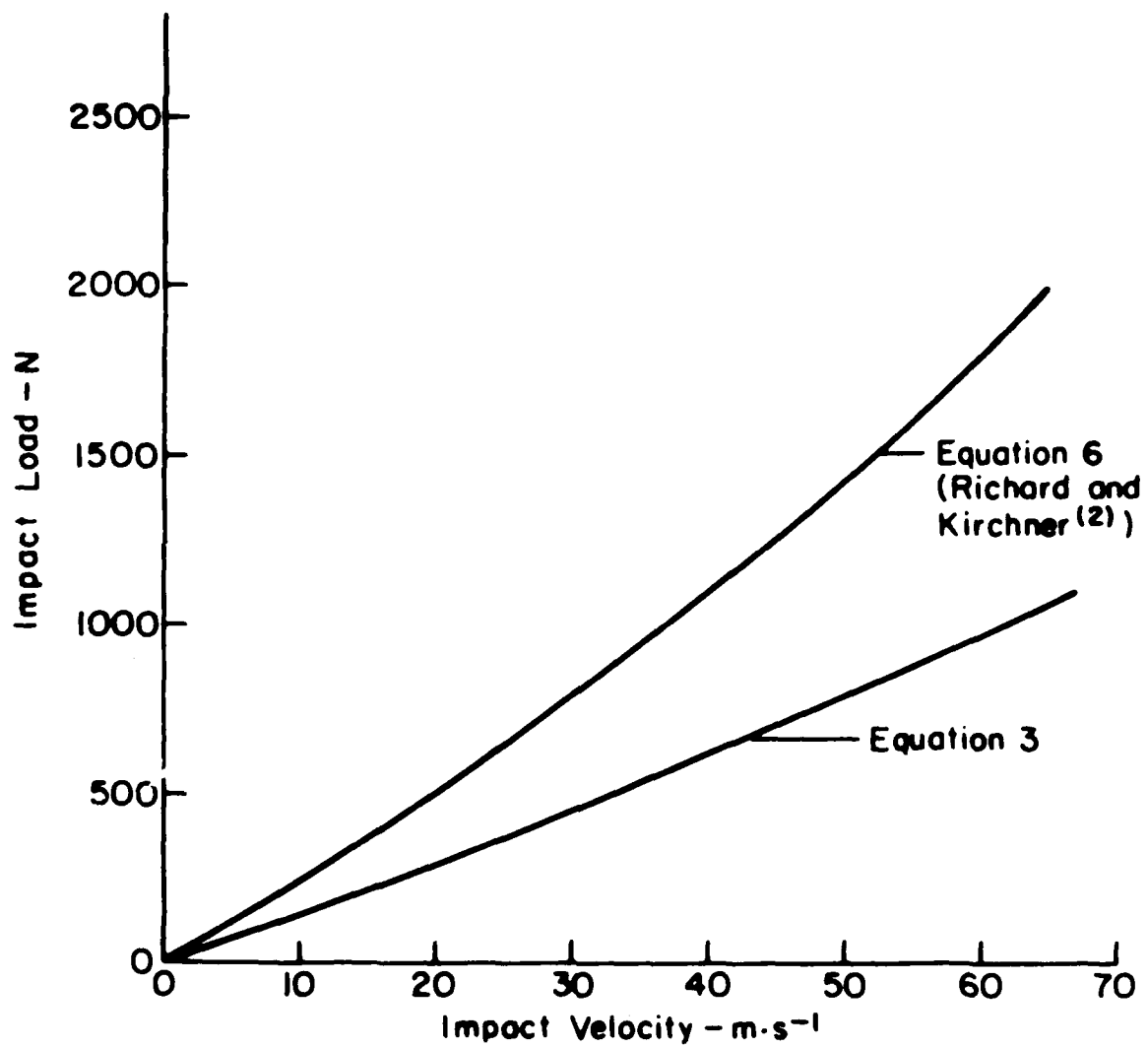


Figure 11 Impact load calculated by two methods vs. impact velocity (ZnS, 3 mm diameter glass spheres).

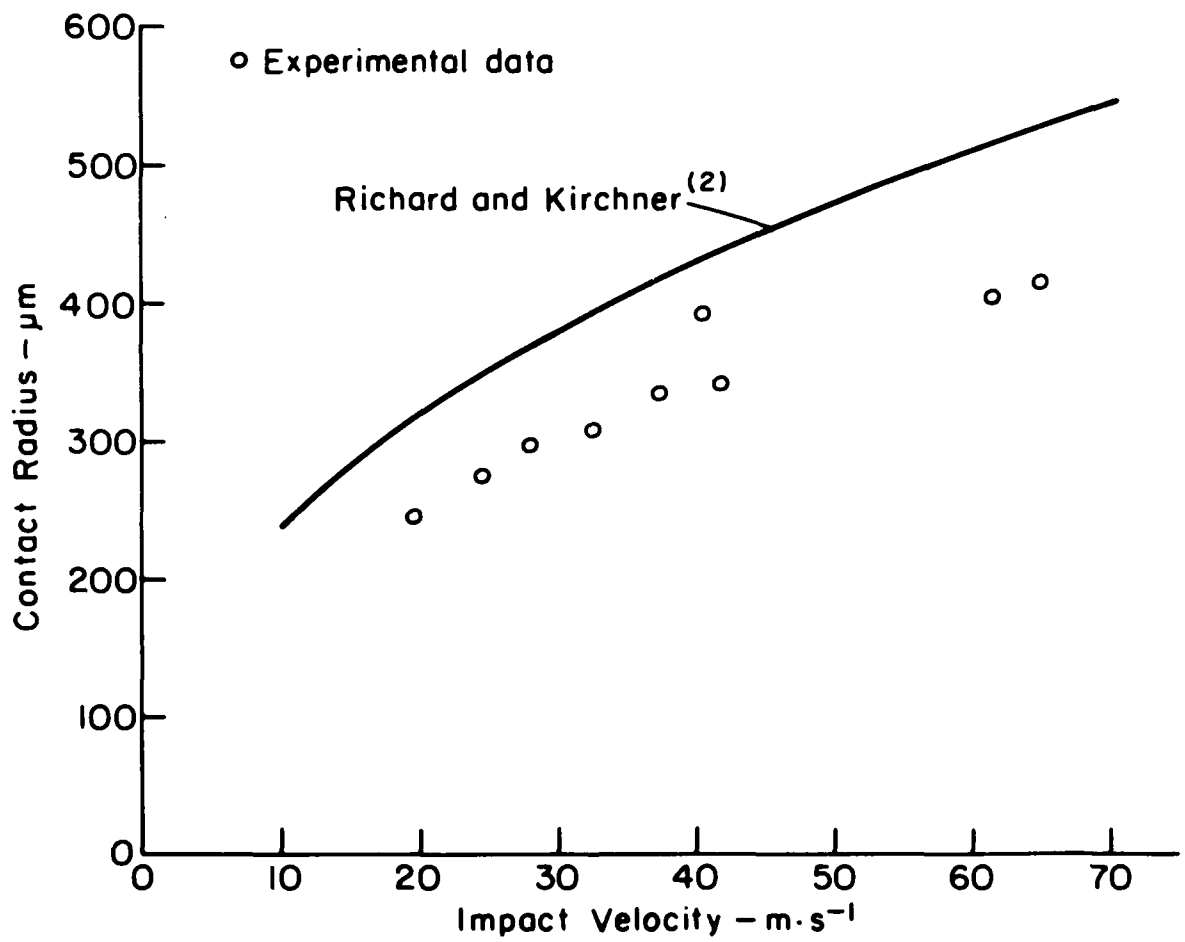


Figure 12 Contact radius vs. impact velocity ZnS, 3 mm diameter glass spheres.

that near the end of the loading cycle, where the maximum load is observed, the flow stress may approach the static, work hardened value.

C. Load dependence of crack length

Examination of Table I shows that several expressions are available relating load and crack length for various assumed conditions. Perhaps the simplest approach was illustrated by Lawn and Fuller⁽⁴⁾ who used an energy balance method to show that, for blunt indenters

$$P \propto K_{IC} c^{3/2} \quad (7)$$

This relation is expected to apply only in the far field; that is, when the crack length is much greater than the contact radius. Also, even though it may describe the situation when the load is applied, it fails to describe crack extension during unloading when residual stresses, originating at the irreversibly deformed zone, substantially alter the stress distributions.

During ceramic machining experiments in which the contact dimension was varied by varying the sharpness or bluntness of the diamond points, it was observed that the penetration of the damage depended strongly on the contact dimension even when the crack length was several times greater than the contact dimension⁽¹⁶⁾. In this particular case, the assumption of line contact loading, as represented by⁽¹⁰⁾

$$P \propto K_{IC} L c^{1/2} \quad (8)$$

in which L is the contact length, yielded a satisfactory comparison of theory and experiment. This was the case despite the fact that the line contact (L) was much smaller than the radial crack length (c). Subsequently, Conway and Kirchner⁽²⁾ analysed propagation of median cracks

beneath an irreversibly deformed (disturbed) zone and found that

$$P \propto K_{IC} z_o c^{\frac{1}{2}} \quad (9)$$

where z_o is the depth of the disturbed zone. Comparisons show that in many cases L and z_o are approximately equal.

Predictions based on (8) and (9) can yield very different results from those based on (7). Therefore, it was of interest to compare these relations with experimental data. Plots of P vs. $c^{3/2}$ and P/d_i vs. $c^{\frac{1}{2}}$ were compared, where d_i is the indentation width which is assumed to replace L or z_o in the above equations.

Damage at static indentations

A satisfactory model relating load and crack length should provide for the following:

1. A load threshold below which cracks do not form.
2. A transition region in which small variations in load cause large variations in crack length as the crack "pops in" and propagates in the near field.
3. A wide range of loads in which crack propagation is governed by a simple relation based on the far field stress distribution.

The results should be evaluated based on these criteria.

The data are plotted as P vs. $c^{3/2}$ and P/d_i vs. $c^{\frac{1}{2}}$ where c is the maximum radial crack length measured along the surface from the edge of the indentation in Figures 13 and 14. The P vs. $c^{3/2}$ curve shows a load threshold. The data points have a much larger slope at low loads than at high loads, indicating that the exponent of c is too high. The near field region is indicated approximately by $c < d_c$ where d_c is the contact diameter. The variation of crack length with load in this region is not

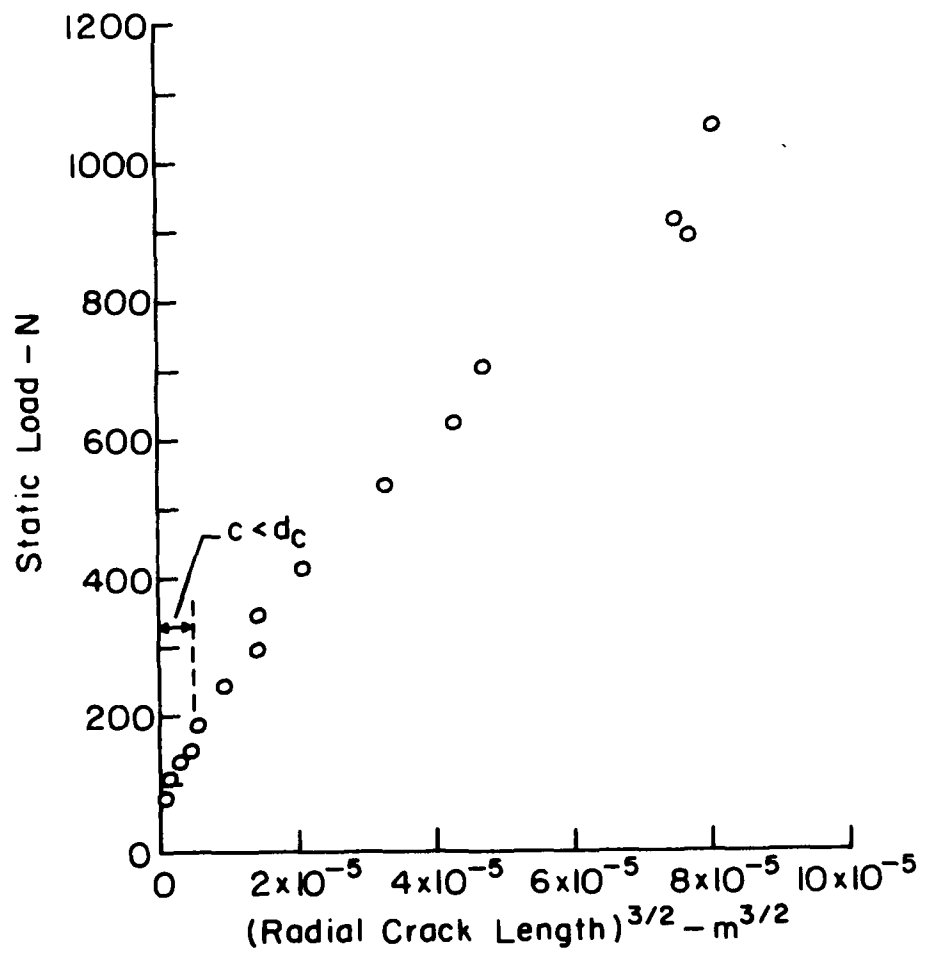


Figure 13 Static load vs. the radial crack length measured from the edge of the indentation and raised to the 3/2 power (ZnS 3 mm diameter glass spheres).

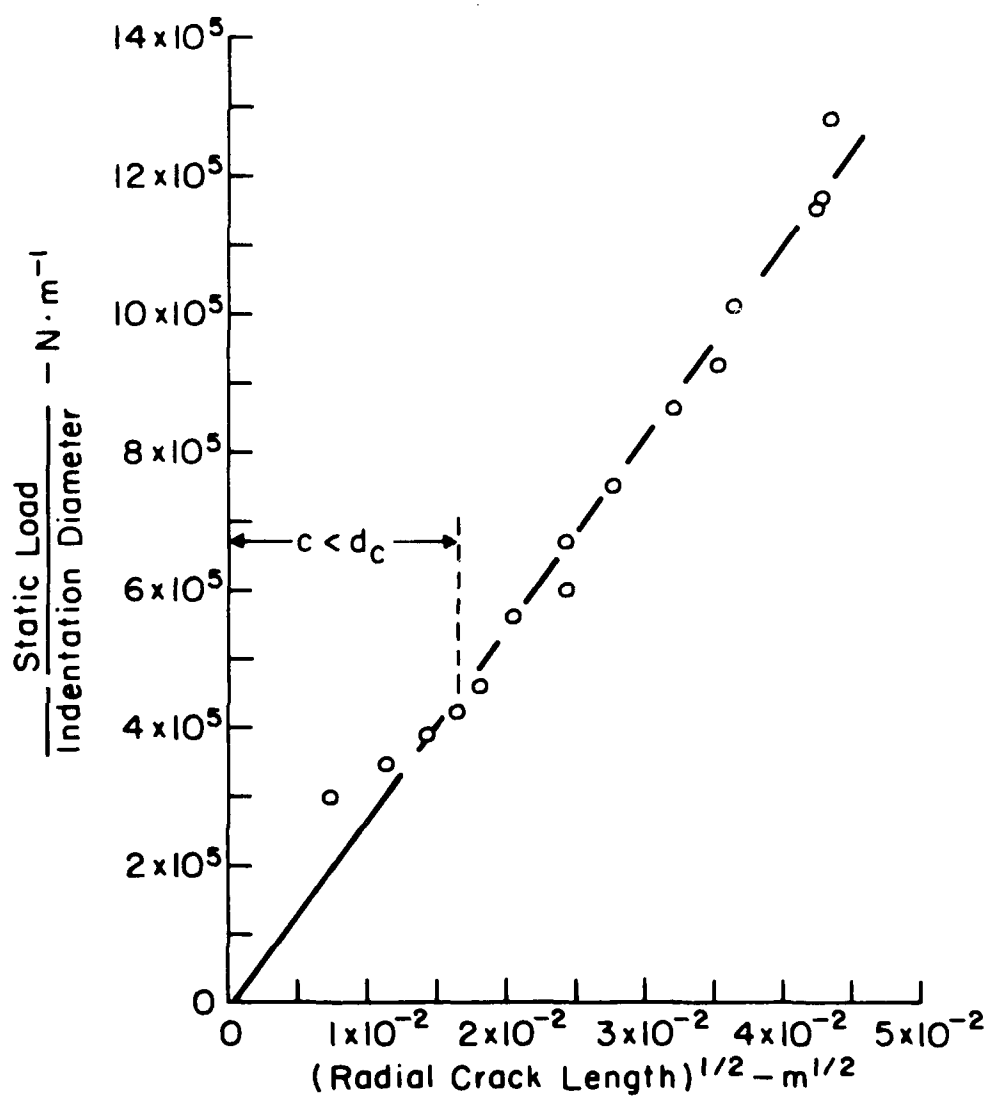


Figure 14. Static load divided by the indentation diameter vs. radial crack length measured from the edge of the indentation and raised to the 1/2 power (ZnS, 3 mm diameter glass spheres).

much different from the rest of the curve.

The P/d_i vs. $c^{\frac{1}{2}}$ curve is much more consistent with the listed criteria. It shows a load threshold, a transition region where $c < d_c$, and an essentially linear dependence in the far field. The coefficient of determination for the data in the far field is 0.98, indicating an excellent fit. These results provide additional experimental confirmation of the earlier results obtained in ceramic machining tests and assuming that $d_i \approx z_o$, they support the analysis of Conway and Kirchner⁽⁹⁾.

Similarly, a P/d_i vs. $c^{\frac{1}{2}}$ curve is given in Figure 15, where c is the radial crack depth measured under the indentations. The results show that the relationship between these variables is approximately linear.

Curves plotted using maximum crack lengths measured from the centers of the indentations were less consistent with the listed criteria.

Damage at impact indentations

The variation of crack length with load at impact indentations was evaluated similarly, using loads calculated by the methods described in Section III B. The results for $P \propto c^{3/2}$ and $P/d_i \propto c^{\frac{1}{2}}$ where c is the radial crack length measured from the edge of the indentation are given in Figures 16 and 17. The P vs. $c^{3/2}$ curves depart substantially from straight lines showing that the exponent 3/2 is much too large. The P/d_i vs. $c^{\frac{1}{2}}$ curves are approximately straight lines that do not pass through the origin. Based on the results for static indentations (Figure 14), one would expect the curve to pass through the origin. The fact that it does not pass through the origin may indicate that the loads in the low part of the load range are overestimated. Also, at the impact sites there may be less crack extension on unloading because of the smaller residual stresses at these sites as a result of the smaller irreversibly deformed zone.

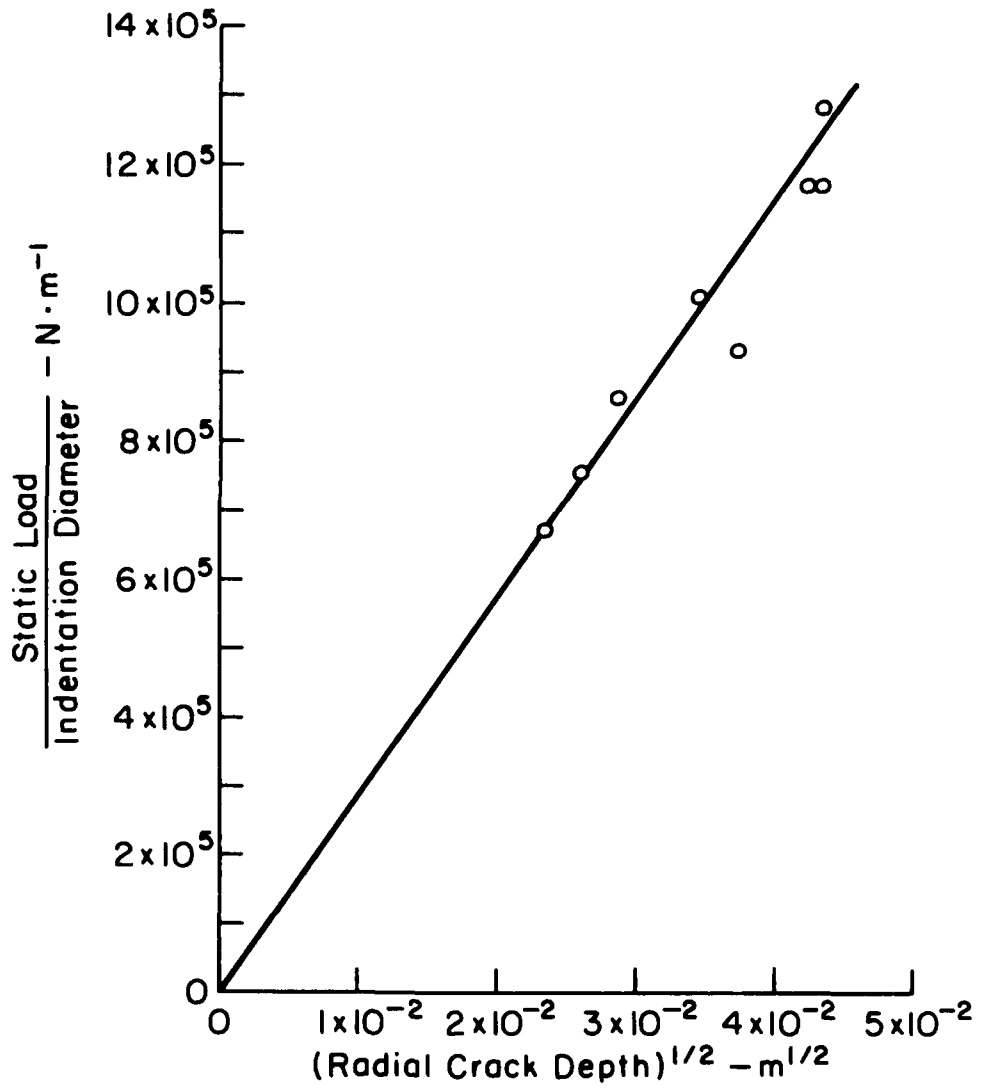


Figure 15 Static load divided by the indentation diameter vs. the radial crack depth raised to the 1/2 power (ZnS, 3 mm diameter glass spheres).

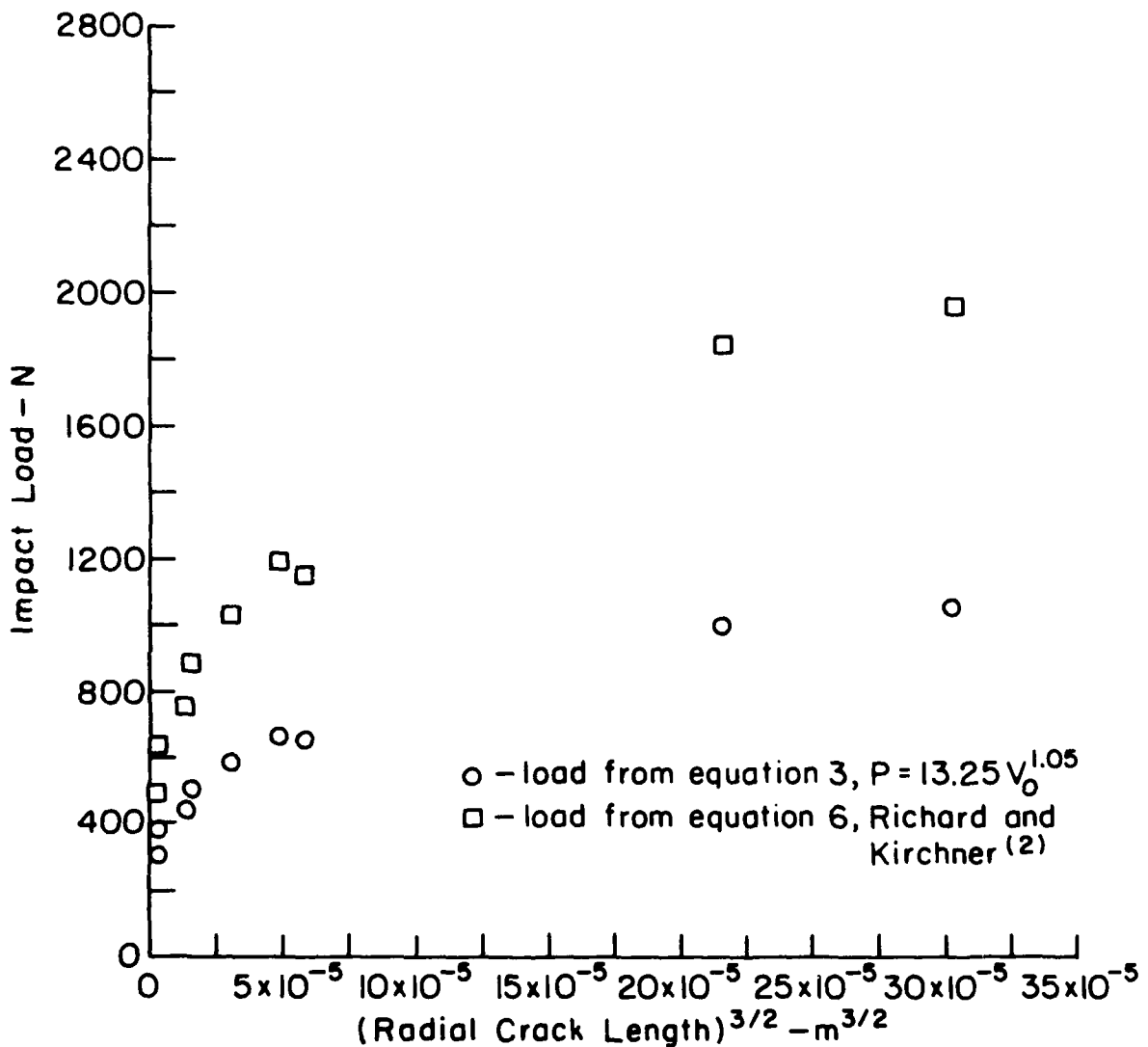


Figure 16 Impact load vs. radial crack length measured from the edge of the indentation and raised to the 3/2 power, for two methods of calculating the impact load (ZnS, 3 mm diameter glass spheres).

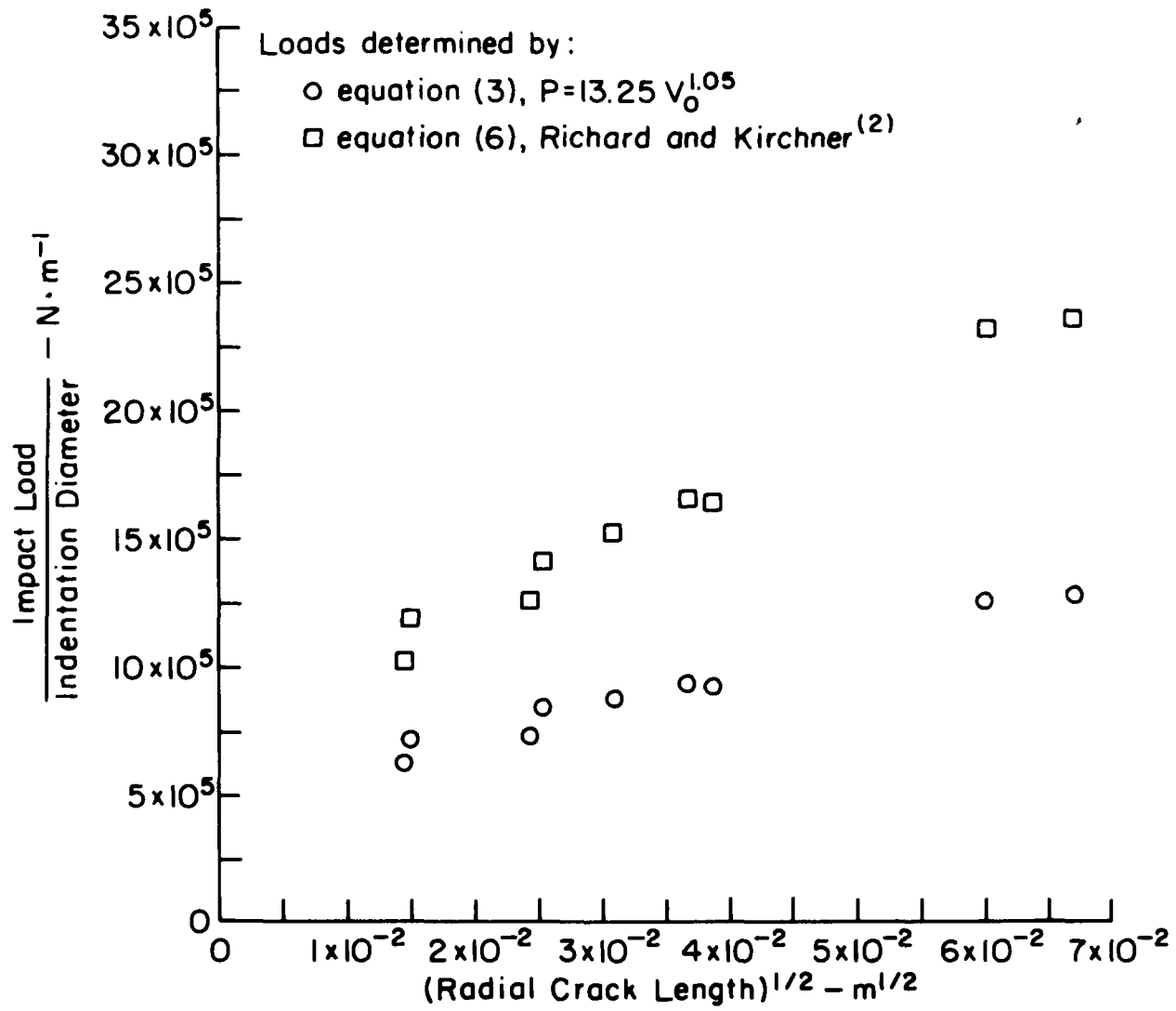


Figure 17 Impact load divided by indentation diameter vs. radial crack length measured from the edge of the indentation and raised to the 1/2 power, for two methods of determining the load (ZnS, 3 mm diameter glass spheres).

No transition region was observed. However, one might not observe the transition region because the minimum loads in the impact tests are greater than those for which the transition was observed in the static tests.

The radial crack depths were measured in several cases. The measurements did not include the depths of median cracks, if present. In some cases, especially for smaller cracks, the measurements were not made because the cracks could not be observed clearly through the edges of the plates. A P/d_i vs. $c^{\frac{1}{2}}$ curve, plotted using loads calculated by the Richard and Kirchner⁽²⁾ method, is presented in Figure 18 showing a linear variation and passing approximately through the origin.

Theoretical crack lengths calculated using the two methods of estimating the loads are compared with experimental data for various impact velocities in Figure 19. The crack lengths used to plot the theoretical curves were calculated by calculating the loads and then substituting these loads in the statically determined relation, $P/d_i = 2.74 \times 10^7 c^{\frac{1}{2}}$, which was obtained by a least squares fit of the data in Figure 14. The results show that, at low impact velocities, crack lengths calculated using $P = 13.25 V_o^{1.05}$ (equation 3) yield the best estimates but at higher velocities the data approach the predictions by the Richard and Kirchner⁽²⁾ method. It seems reasonable that equation (3) would yield its best results at low velocities because momentum and energy effects which are neglected in this case should be less important in this velocity range. It also seems reasonable that the Richard and Kirchner method might yield better results than equation (3) at higher impact velocities because momentum and energy effects are accounted for in this derivation. However, it is not clear why the Richard and Kirchner

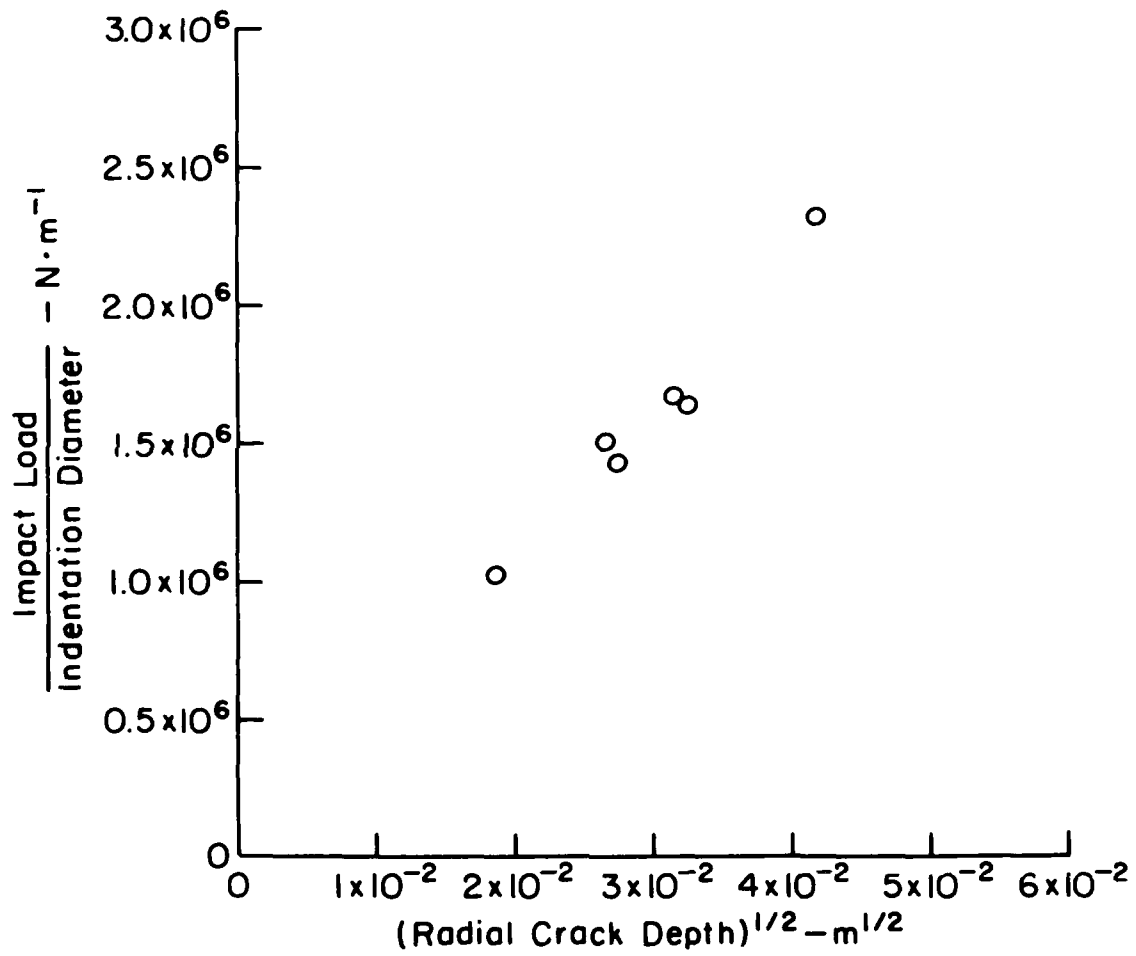


Figure 18 Impact load divided by indentation diameter vs. radial crack depth to the 1/2 power (impact load predicted using equation (6); ZnS, 3 mm diameter glass spheres).

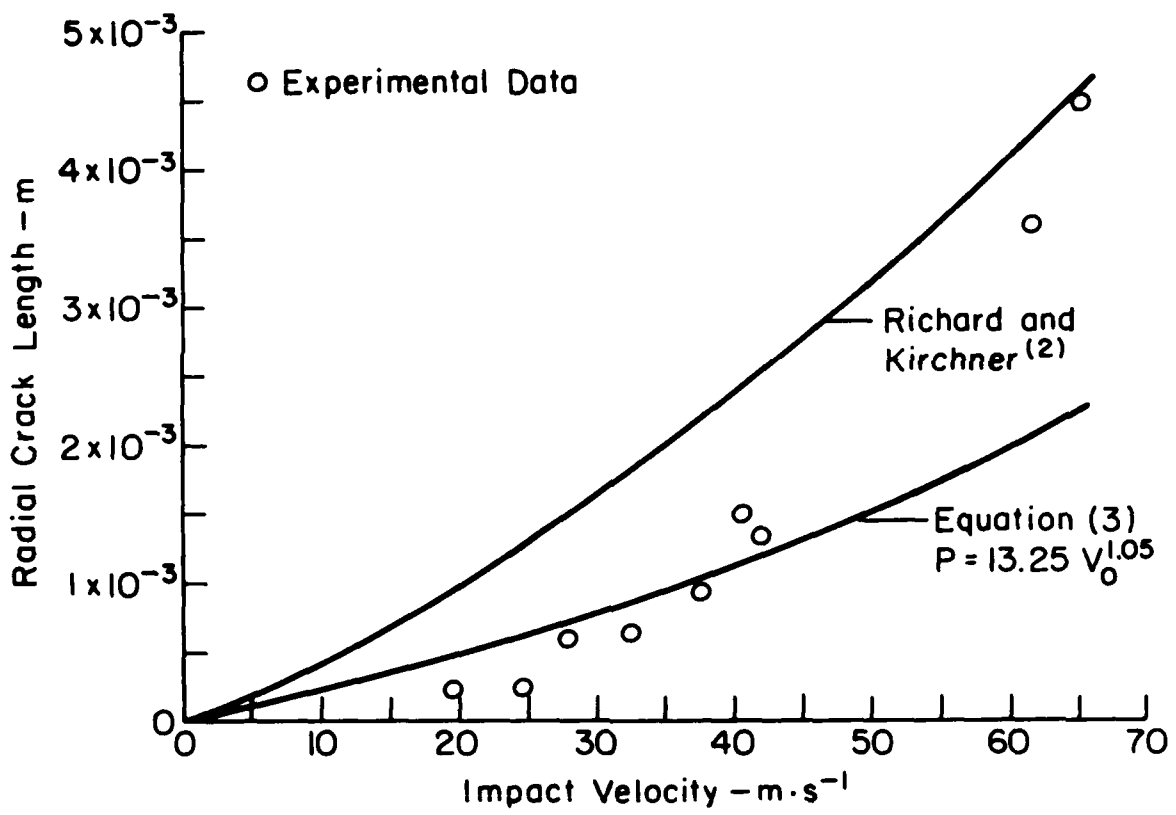


Figure 19 Comparison of two theoretical curves of radial crack length vs. impact velocity with experimental data using c measured from the edge of the indentation. (ZnS, 3 mm diameter glass spheres).

method overestimates the crack lengths by such a wide margin at low velocities.

D. Energy losses

The various energy loss mechanisms during elastic-plastic impact on materials include the indentation energy, stress wave energy and the fracture energy absorbed by formation of new surfaces. Previous research has shown that the stress wave and fracture energy losses are not particularly important factors^(12,17). Hunter⁽¹⁸⁾ predicted that for elastic conditions the kinetic energy loss should increase as the 2.6 power of the impact velocity as a result of stress wave energy losses. Kirchner and Cruver⁽¹⁹⁾ found that for impacts of glass spheres on glass plates at temperatures below the softening point, the measured kinetic energy loss variation was very close to Hunter's prediction. At temperatures above the softening point where indentation energy became important, the energy losses increased but the velocity dependence remained very much the same.

The kinetic energy loss vs. impact velocity data for impacts of glass spheres on zinc sulfide plates is given in Figure 20. The slope is 2.94 at the higher velocities and the indications are that the slope is even higher at low velocities. Therefore, the kinetic energy losses increase more rapidly with velocity in ZnS than they do in glass. This more rapid increase may occur because of broadening of the load vs. penetration curve with increasing impact velocity that can occur as a result of the strain rate dependence of the flow stress.

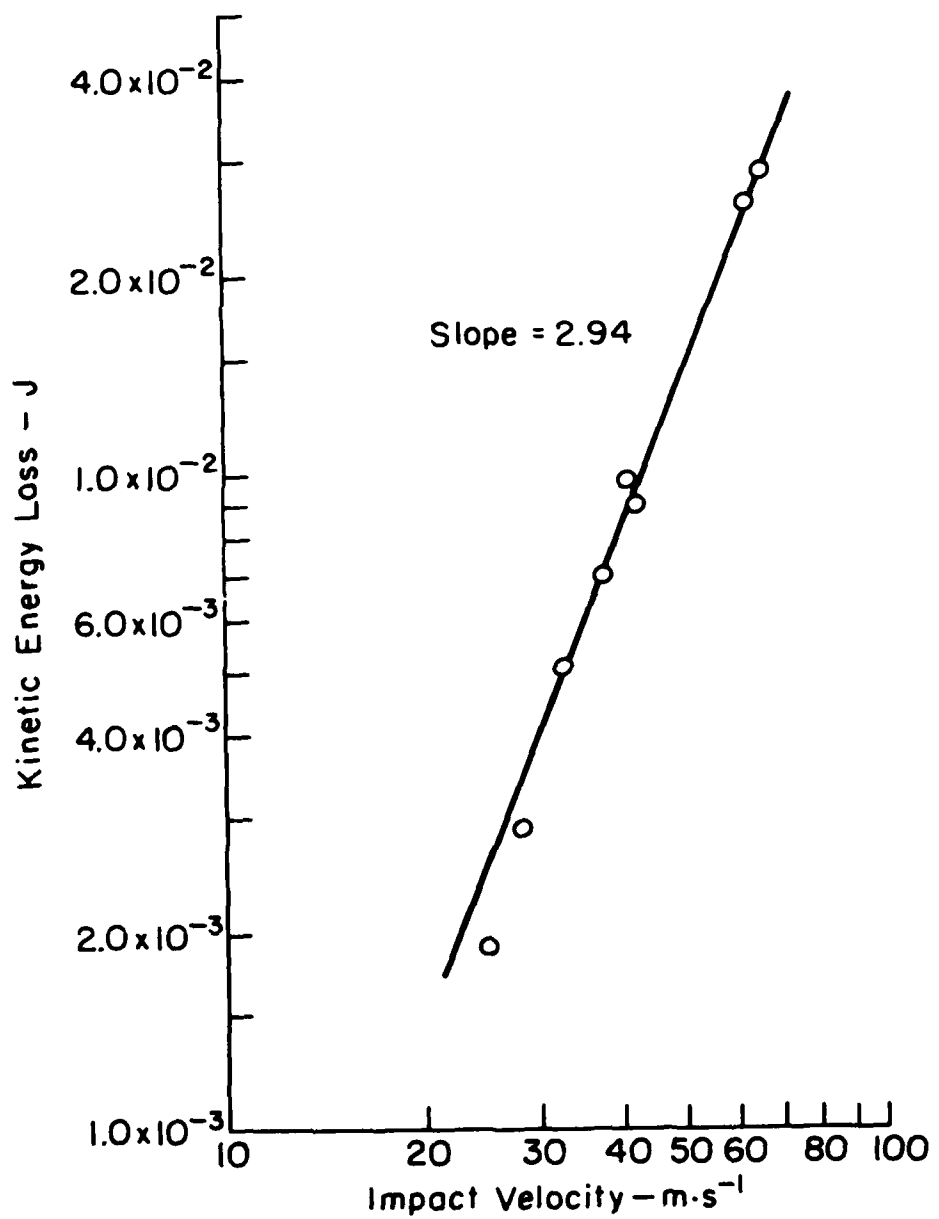


Figure 20 Kinetic energy loss vs. impact velocity (ZnS, 3 mm diameter glass spheres).

IV. SUMMARY AND CONCLUSIONS

ZnS plates were statically indented under various loads and impacted at various velocities using 3 mm diameter glass spheres. The contact damage was characterized and the damage at the static and impact sites was compared with the results described in the previous section.

Damage at the static and impact indentations included the irreversibly deformed zone directly under the indentation and circumferential ring, radial, and lateral cracks. The scale of the damage at the static indentations increased with increasing loads on the glass spheres. An overall comparison of the static and impact damage at approximately equal indentation radii, as shown in Figure 3, shows that the scale of the impact damage is approximately the same as that of the static indentation damage. If one assumes that the sizes of the cracks depend primarily on the maximum loads applied at the contact, this observation appears to justify the original assumption of equal loads at equal indentation radii for static and impact indentations. However, the detailed observations show that there are substantial differences in the indentation radius thresholds for crack formation and the numbers and sizes of the cracks at static and impact indentations so that other factors are important.

At equal indentation radii, the impact indentations were shallower than the static indentations showing that less irreversible deformation had occurred at the impact sites. Because less irreversible deformation had occurred, the threshold indentation radius for formation of radial cracks was shifted to higher indentation radii and fewer radial cracks were formed. Also, at smaller indentation radii the radial cracks at static indentations were longer than those at impact sites. At the largest

indentation radii the reverse was true.

When compared on the same basis, lateral cracks were initiated first at impact sites and were only observed at the static sites with the three largest indentation radii. At these three static sites, the lateral cracks were shorter than those at the comparable impact sites. The lateral cracks are considered to form mainly in response to the in-plane hoop stresses. Therefore, the longer lateral cracks at the impact sites indicate that the in-plane hoop stresses are greater in the impact case.

Several mathematical models are available that can be used to predict the lengths of cracks depending on the load applied during contact.

In the case of static loading two of these models, $P \propto C^{3/2}$ and $P/d_i \propto C^{\frac{1}{2}}$, were compared with experiment by plotting the data and determining the intercepts and linearity of the resulting plots. $P/d_i \propto C^{\frac{1}{2}}$ yielded the best results. Linear extrapolations using $P \propto C^{3/2}$ greatly underestimated the crack lengths at high loads. The good results using $P/d_i \propto C^{\frac{1}{2}}$ indicate that the characteristics of the contact have a substantial influence on the extent of crack propagation. The mechanism responsible for this influence remains uncertain. The dimensions of the contact, depth of the disturbed zone, wedging, and residual stresses may be important factors influencing the extent of damage.

In order to make a similar evaluation in the impact case, it was necessary to estimate the loads. Three methods were used, each yielding substantially different results. However, in this case also, plotting the data using P/d_i vs. $C^{\frac{1}{2}}$ yielded the best results.

To predict strength degradation, erosion rates and loss of transmission due to reflections at lateral cracks, it is necessary to predict the extent of crack propagation for various impact conditions. The present results show that for impacts of 3 mm glass spheres on zinc sulfide

at velocities up to $65 \text{ m}\cdot\text{s}^{-1}$, the characteristics of the contact zone have an important influence in the extent of crack propagation, even in the far field.

LIST OF SYMBOLS

P	- Maximum load perpendicular to surface
c	- Crack length
K_{IC}	- Critical stress intensity factor
$k(\nu)$	- Dimensionless function of Poisson's ratio ν
H	- Hardness (pressure)
χ	- Proportionality factor accounting for unknown geometrical and frictional factors
χ_r	- χ for residual stress field after removal of load
β	- Geometrical factor determined by inelastically deformed zone
α	- Geometrical factor determined by indenter
$\psi(\nu)$	- $\psi(\nu) \approx (1-\nu^2) (1-2\nu)^2 / 2\pi^4$ where ν is Poisson's ratio
r_c	- Contact radius
r_o	- Radius of impacting sphere
E	- Young's modulus
Q	- $Q = f(\nu, E)$
v_o	- Impact velocity
Ω	$\Omega = \kappa \pi r_o^2 \left[\frac{M (\xi+4)}{2 \kappa \pi r_o^3} \right]^{\frac{\xi+2}{\xi+4}}$ where M is mass of impacting sphere and κ and ξ are contact parameters
z_o	- Depth of "disturbed" zone
L	- Contact length
χ_L	- χ for line loading
p_r	- Residual load caused by irreversible deformation during loading
r_i	- Indentation radius
d_i	- Indentation diameter

Symbols (continued)

d_c	- Contact diameter
Δ	- Depth of the indentation
W_{pl}	- Plastic energy (energy of plastic deformation)
$f(E)$	$- \frac{1-\nu_1^2}{E_1} + \frac{1-\nu_2^2}{E_2}$
E_1	- Young's modulus of projectile
E_2	- Young's modulus of plate
ν_1	- Poisson's ratio of the projectile
ν_2	- Poisson's ratio of the plate
η	- Contact pressure
η'	- Indentation pressure
η_d	- Impact pressure
A	- Area
κ	- Resistance to penetration
ξ	- Exponent characteristic of the variation of the pressure of contact with increasing load
κ'	- Resistance to indentation
ξ'	- Exponent related to work hardening
ρ_1	- Density of projectile
ρ_2	- Density of plate

ACKNOWLEDGEMENTS

The writers are pleased to acknowledge the contributions of their associates at Ceramic Finishing Company, especially J. C. Conway and D. M. Richard and the sponsorship of the Office of Naval Research.

REFERENCES

1. A. G. Evans and T. R. Wilshaw, "Quasi-Static Solid Particle Damage in Brittle Solids, I, Observations, Analyses and Implications," *Acta Met.* 24, 939-956 (1976).
2. D. M. Richard and H. P. Kirchner, "Theory of Elastic-Plastic Impact on Ceramics," presented at the Fifth International Conference on Erosion by Liquid and Solid Impact, Cambridge, England (Sept. 4, 1979) Published in the Proceedings of the Conference, pages 27-1 to 27-10.
3. D. A. Shockley, K. C. Dao and D. R. Curran, "Nucleation and Growth of Cracks in CVD ZnS Under Particle Impacts," SRI International Annual Report, Part II, Contract N00014-76-C-0657 (April, 1979).
4. B. R. Lawn and E. R. Fuller, "Equilibrium Penny-like Cracks in Indentation Fracture," *J. Mater. Sci.* 10, 2016-2024 (1975).
5. F. C. Roesler, "Brittle Fractures Near Equilibrium," *Proc. Phys. Soc. B* 69, 981-992 (1956).
6. B. R. Lawn and R. Wilshaw, "Indentation Fracture: Principles and Applications," *J. Mater. Sci.* 10, 1049-1081 (1975).
7. D. B. Marshall and B. R. Lawn, "Residual Stress Effects in Sharp Contact Cracking, Part I Indentation Fracture Mechanics," *J. Mater. Sci.* 14, 2001-2012 (1979).
8. A. G. Evans, "Strength Degradation by Projectile Impacts," *J. Amer. Ceram Soc.* 56 (8) 405-409 (1973).
9. J. C. Conway and H. P. Kirchner, "The Mechanics of Crack Initiation and Propagation Beneath a Moving Sharp Indenter," To be published in *J. Mater. Sci.*
10. B. R. Lawn and D. B. Marshall, "Contact Fracture Resistance of Physically and Chemically Tempered Glass Plates: A Theoretical Model," *Phys. Chem. Glasses* 18 (1) 7-18 (1977).
11. H. Tada, P. C. Paris and G. R. Irwin, "The Stress Analysis of Cracks Handbook," Del Research Corp. Hellertown, PA (1973).
12. I. M. Hutchings, "Energy Absorbed by Elastic Waves During Plastic Impact," *J. Phys. D: Applied Physics* 12 (11) 1819-24 (November, 1979).
13. J. D. Campbell, "Dynamic Plasticity: Macroscopic and Microscopic Aspects," *Mater. Sci. and Eng.* 12, 3-21 (1973).
14. I. M. Hutchings, "Strain Rate Effects in Microparticle Impact," *J. Phys. D: Applied Physics* 10, L179 - L184, 1977.

15. D. Tabor, "The Hardness of Metals," The Clarendon Press (1951).
16. H. P. Kirchner, R. M. Gruver and D. M. Richard, "Fragmentation and Damage Penetration During Abrasive Machining of Ceramics" from The Science of Ceramic Machining and Surface Finishing II, Edited by B. J. Hockey and R. W. Rice, NBS Special Publication 562 (October, 1979) pages 23-42.
17. H. P. Kirchner and R. M. Gruver, "The Effect of Localized Damage on Energy Losses During Impact," Mater. Sci. Eng. 33, 101-106 (1978).
18. S. C. Hunter, "Energy Absorbed by Elastic Waves During Impact," J. Mech. Phys. Solids 5, 162-171 (1957).
19. H. P. Kirchner and R. M. Gruver, "Localized Impact Damage in a Viscous Medium (Glass)," from Fracture Mechanics of Ceramics, Vol. 3, Edited by R. C. Bradt, D. P. H. Hasselman and F. F. Lange, Plenum, New York (1978) pages 365-377.

APPENDIX A

COMPARISON OF THE THREE IMPACT LOAD EQUATIONS

A. Hutchings' impact load equation

Hutchings⁽¹⁾ derived his impact load equation by assuming that during contact the sphere remains rigid and the material responds perfectly plastically (no elastic response and no work hardening). These assumptions enable Hutchings to use a constant indentation pressure, (η_d), in the equation of motion of the sphere. The solution of this equation of motion yields a relation for the load on the sphere as a function of contact time. We are interested in the maximum load, which was found to be

$$P = \frac{4}{3} \pi r_o^2 \rho_1 v_o (3\eta_d/2\rho_1)^{\frac{1}{2}}. \quad (1)$$

By substituting for the density of the sphere, (ρ_1), its mass divided by its volume ($3M/4\pi r_o^3$), equation (1) becomes

$$P = (2\pi r_o M \eta_d)^{\frac{1}{2}} v_o. \quad (2)$$

B. Comparison of Hutchings' Equation with that of Richard and Kirchner

Richard and Kirchner⁽²⁾ also assumed that the sphere remained rigid during contact, but in order to account for the elastic-plastic response of the material and the effects of work hardening, they assumed that the pressure was related to the contact radius by

$$\eta = \kappa (r_c/r_o)^{\frac{6}{5}}. \quad (3)$$

Then, by equating the kinetic energy of the sphere to the work done by

the sphere in reaching maximum penetration, the impact load equation was found to be

$$P = k \pi r_o^2 \left[\frac{M(\xi+4)}{2k \pi r_o^3} \right]^{\frac{(\xi+2)}{\xi+4}} v_o^{2\left(\frac{\xi+2}{\xi+4}\right)}. \quad (4)$$

If the assumptions made by Hutchings are applied to equation (3), ξ becomes zero, and k then equals a constant indentation pressure, η_d . Making these substitutions for ξ and k , equation (4) becomes

$$P = \eta_d \pi r_o^2 \left[\frac{4M}{2\eta_d \pi r_o^3} \right]^{\frac{1}{2}} v_o^{2(\frac{1}{2})}. \quad (5)$$

which reduces to

$$P = (2\pi r_o M \eta_d)^{\frac{1}{2}} v_o. \quad (6)$$

Thus, the impact load equation of Richard and Kirchner reduces to Hutchings' equation for the ideal case of a rigid sphere and a perfectly plastic material response.

C. Comparison of the three impact load relations

To see how the inclusion of elastic-plastic response and work hardening affects the impact load, equations (2) and (4) were evaluated and compared. To evaluate equation (2), the hardness ($H = 1.90$ GPa⁽³⁾) was substituted for η_d . Thus equation (2) reduces to

$$P = 25.2 v_o. \quad (7)$$

When the experimental values for ξ and k are substituted into equation (4), we get

$$P = 16.1 v_o^{1.15}. \quad (8)$$

Equations (7) and (8) are plotted in Figure 1. For velocities up to about $25 \text{ m}\cdot\text{s}^{-1}$, equation (7) is a good linear approximation for equation (8). At higher velocities the higher velocity exponent in equation (8) results in increasingly higher loads than equation (7).

Also plotted in Figure 1 is the empirical relation

$$P = 13.25 v_0^{1.05} \quad (9)$$

which was derived in the main body of the report. This relation yields much lower impact loads than equations (7) and (8). It should be pointed out that the effects of work hardening and an elastic-plastic material response as they pertain to static loading are contained implicitly in equation (9).

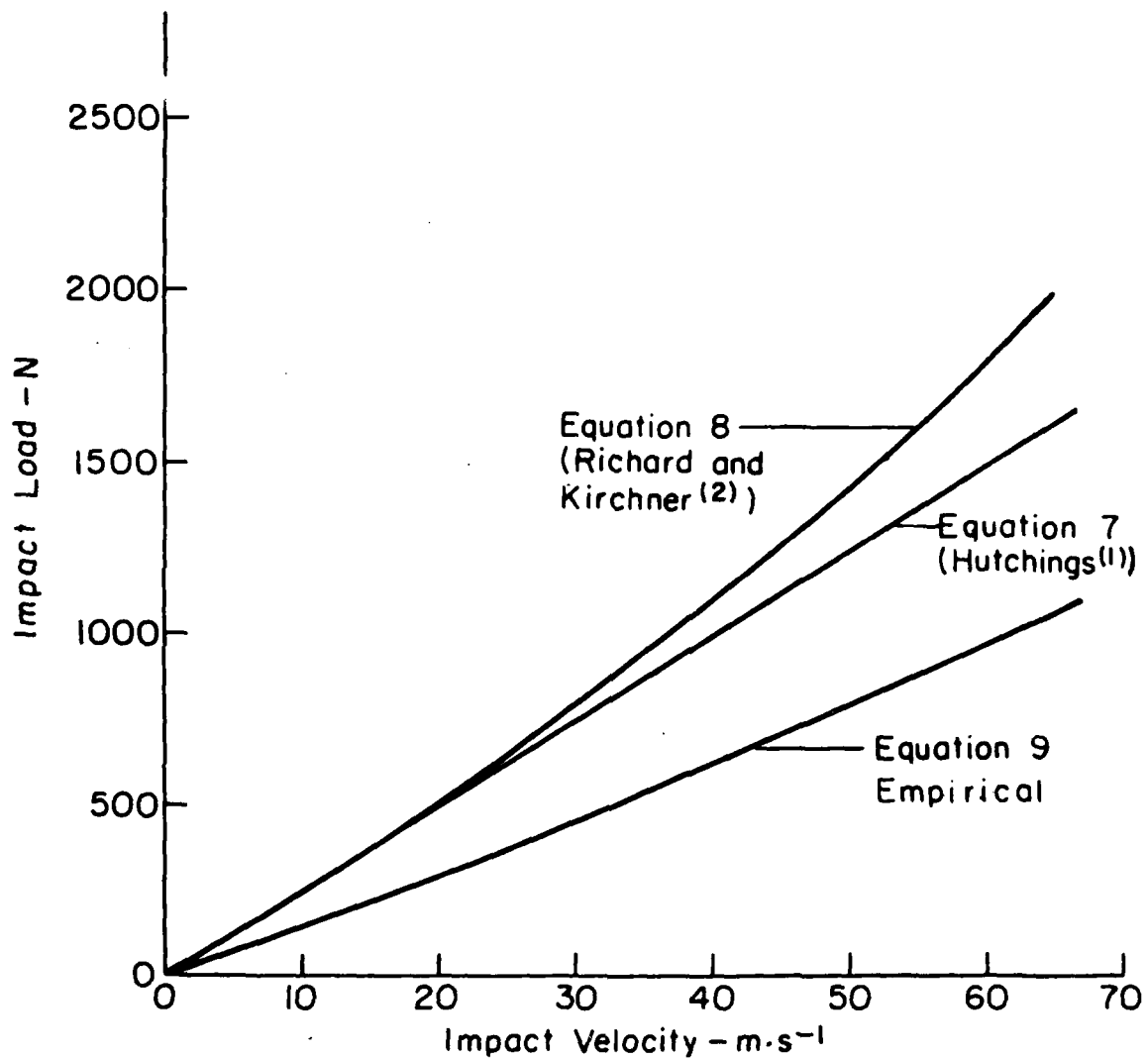


Figure 1 Impact load calculated by three methods vs. impact velocity (ZnS, 3 mm diameter glass spheres).

CONCLUSION

Since ZnS exhibits an elastic-plastic response with significant work hardening under static loading, it was decided to use equations (8) and (9) which account for these effects, in the analysis of the impact load versus crack length relations. Equation (7) was not used since it is merely an idealized case of equation (8).

REFERENCES

1. I. M. Hutchings, "Energy Absorbed by Elastic Waves During Plastic Impact," *J. Phys. D: Applied Physics* 12 (11) 1819-24 (November, 1979).
2. D. M. Richard and H. P. Kirchner, "Theory of Elastic-Plastic Impact on Ceramics," presented at the Fifth International Conference on Erosion by Liquid and Solid Impact, Cambridge, England (Sept. 4, 1979), Published in the Proceedings of the Conference, pages 27-1 to 27-10.
3. A. G. Evans and T. R. Wilshaw, "Quasi-Static Solid Particle Damage in Brittle Solids, I, Observations, Analysis, and Implications," *Acta Met.* 24, 939-956 (1976).

Crack Growth from Small Flaws in Larger Grains in Alumina

by

H. P. Kirchner
J. M. Ragosta

Ceramic Finishing Company
P.O. Box 498
State College, PA 16801

Abstract

Crack growth in alumina was simulated for the case of small flaws in larger surface crystals to determine the range of crystal sizes and loading rates in which single crystal fracture energies would be expected to control fracture. This should be expected only for large crystals and very high loading rates.

I. Introduction

It has been pointed out by Rice and co-workers (1-4) that, when fractures originate at relatively small flaws in large grains in polycrystalline ceramics, fracture may be controlled by single crystal fracture energies rather than the fracture energy of the polycrystalline body. Comparisons of fracture energies calculated from measured flaw sizes assuming negligible subcritical crack growth, with fracture energies measured on large cracks, were used to support their viewpoint. The calculated fracture energies frequently were smaller than the measured values. However, using

$$K_{Ic} = (2E\gamma_c)^{1/2} = Y\sigma_F a_c^{1/2} \quad (1)$$

in which K_{Ic} is the critical stress intensity factor, E is Young's modulus of elasticity, γ_c is the critical fracture energy, Y is a geometrical constant that accounts for the shape and location of the crack, σ_F is the fracture stress, and a_c is the strength controlling dimension of the crack, one can see that, if subcritical crack growth occurs, a_c is underestimated, so that it is uncertain whether or not the difference in the fracture energies represents physical reality or the result of an incorrect assumption about subcritical crack growth.

Recently, Singh et al. (5) investigated the relationship of flaw size and grain size to the strength of ceramics. They concluded that in most ceramics an initial flaw contained within a single large grain will

initially propagate and then arrest after entering the region of increased fracture surface energy. However, their analysis also neglected to account for subcritical crack growth.

Calculations of subcritical crack growth for glass and alumina in water at room temperature have shown that very high loading rates, close to those characteristic of Charpy impact tests, are necessary to limit subcritical crack growth to negligible values under these conditions (6). Therefore, the assumption of negligible subcritical crack growth requires further evaluation. In this investigation subcritical crack growth calculations were used to determine the conditions at failure in specimens in which the flaw at the fracture origin was smaller than the particular crystal at the origin and the size of the crystal was varied over a wide range. Loading rates were varied from 10^{-1} to 10^8 MPas $^{-1}$ and included delayed fracture tests. The procedures are described in the next section.

III. Procedures

Selection of data for calculations

In order to provide a quantitative theoretical basis for judging the importance of subcritical crack growth in determination of fracture energies from experimentally measured fracture stresses and flaw sizes, subcritical crack growth was calculated for small flaws in larger grains of various sizes under various loading conditions. These calculations were done by numerical integrations involving the equation

$$V = A K_I^n$$

in which V is the crack velocity, K_I is the stress intensity factor, and A and n are constants for a particular material and set of test conditions.

Alumina was the only material for which suitable data (values of A , n , and K_{Ic}) were known to be available for a single crystal and a polycrystalline body of the same material, measured at the same temperature and humidity. The data of Wiederhorn (7,8) for sapphire and Evans (8,9) for a coarse grained (25 μm average grain size (10)) polycrystalline alumina body met these conditions in the case of measurements at 30% relative humidity. However, preliminary calculations revealed that

*Despite the fact that the choice of alumina was necessary, it is subject to certain disadvantages. The principal disadvantage is that the thermal expansion anisotropy of corundum gives rise to localized residual stresses that are not accounted for in the analysis.

subcritical crack growth was very important for this particular case primarily because there is such a large difference between the K_I at which significant crack growth begins in the sapphire ($K_I = 1.0 \text{ MPam}^{1/2}$) and the K_{Ic} of the polycrystalline body ($K_{Ic} = 5.4 \text{ MPam}^{1/2}$). Because the above data represent a particularly unfavorable case for evaluation of the hypothesis involving the possibility of fracture of polycrystalline bodies at single crystal fracture energies, a second set of data was calculated for a fine grained alumina body with a substantially lower K_{Ic} . The body selected was a 96% alumina. Values of n and A for Region I were estimated using the data of Freiman, McKinney, and Smith (2) that apparently were taken at 40% relative humidity. The transition region (Region II) which is mainly determined by geometry and humidity was assumed to occur at the same crack velocity as that for Evans' coarse grained alumina. K_{Ic} was assumed to be the same as that measured by Bansal, Duckworth, and Niesz (11) for the same alumina fractured under water. Because of the high crack velocity, the presence of the water should not have a significant effect on the K_{Ic} value. Even though the conditions used in the three investigations from which the data were taken for the fine grained alumina calculations are not entirely self consistent, these data have enabled us to compare results for two aluminas with differing K_{Ic} values. The data are given in Figure 1 and Table I*.

General description of assumed crack propagation conditions

For the growth of the flaw within the crystal at the fracture origin, the velocities were estimated using an approximation of the relationship

* The symbols SCI, SCII, SCIII, and PCI, PCII, PCIII refer to Regions I, II, and III for single crystals and polycrystals, respectively.

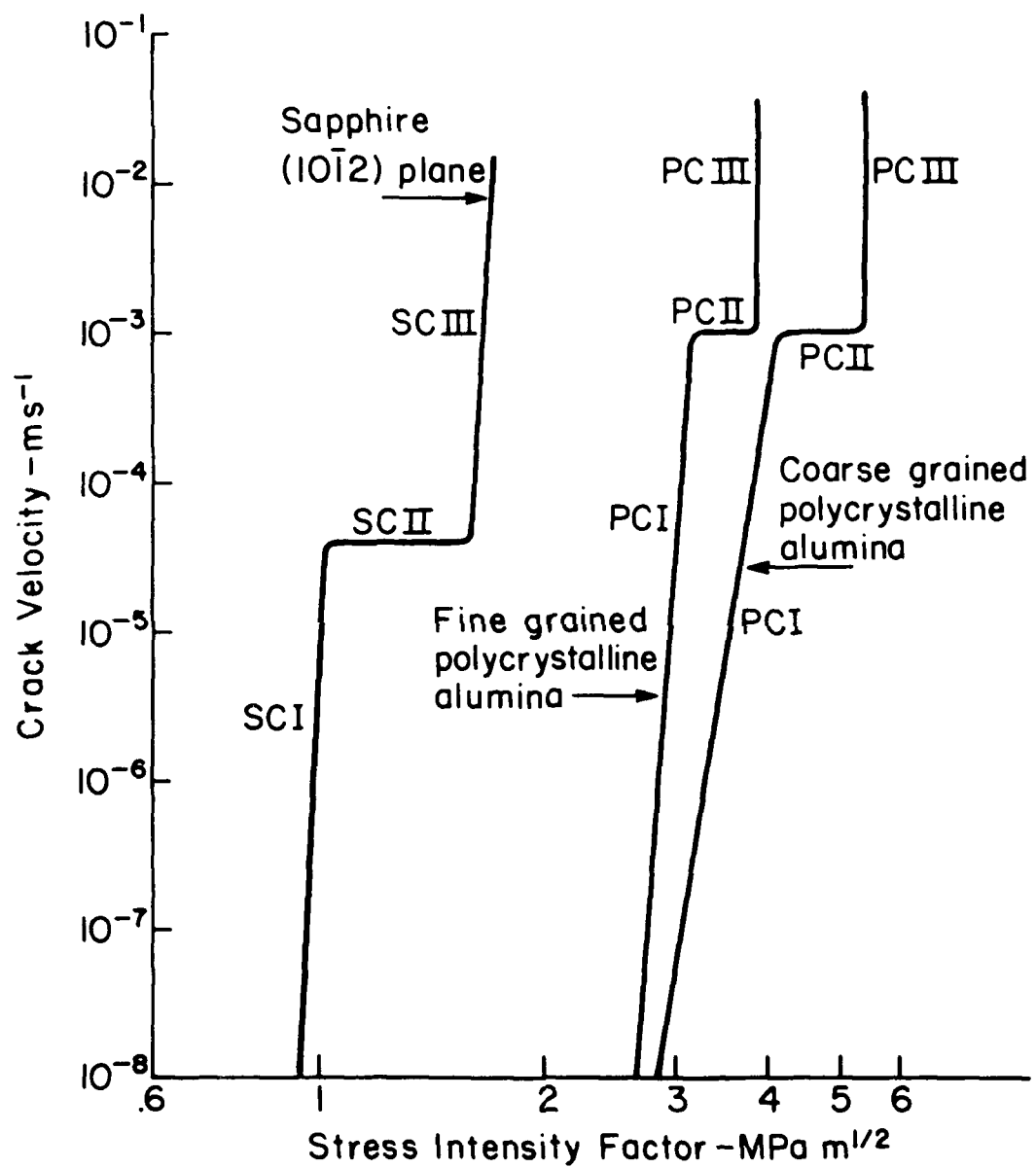


Figure 1 Crack velocity vs. stress intensity factor for single crystal and polycrystalline alumina

Table I
Values of n , A and the end points used for
subcritical crack growth calculations

Material	Crack Growth Region	n	A	End Point
Coarse grained alumina (1)	SC I	112.70	$1.07 \cdot 10^{-5}$	$K_T = 1.02$
	SC II	0.00	$4.00 \cdot 10^{-5}$	$K_T = 1.6$
	SC III	66.89	$5.12 \cdot 10^{-19}$	Crystal Boundary
	PC I	33.00	$4.98 \cdot 10^{-24}$	$K_T = 4.12$
	PC II	0.00	0.001	$K_{Te} = 6.4$
Fine grained alumina (2)	SC I	112.70	$1.07 \cdot 10^{-5}$	$K_T = 1.02$
	SC II	0.00	$4.00 \cdot 10^{-5}$	$K_T = 1.6$
	SC III	66.89	$5.12 \cdot 10^{-19}$	Crystal Boundary
	PC I	51.40	$1.12 \cdot 10^{-30}$	$K_T = 3.34$
	PC II	0.00	0.001	$K_{Te} = 3.84$

Note (1) HYALUMINA, 95% alumina, 25 μm average grain size

Note (2) ALSIMAG 614, 96% alumina, 5 μm average grain size,
3 M Company, Chattanooga, Tennessee

between crack velocity V and stress intensity K_I depicted in the curve (Figure 1) for sapphire. When the crack reached the boundary of the crystal, the crack growth was assumed to be governed by one or the other of the curves for the polycrystalline materials. Whether or not the assumption of an abrupt transition from single crystal to polycrystal propagation conditions is realistic may depend to a great extent on the size of the crystal in which the fracture originates at the fracture origin and the variations in the degree of preferred orientation near the fracture origin. To take some specific examples, a 50 μm grain at the fracture origin in a body with a 5 μm average grain size will probably be surrounded by many grains so that assumption of an abrupt transition may be reasonable. However, a 50 μm grain at the fracture origin in a body with a 25 μm average grain size will be surrounded by a relatively smaller number of grains. Considering the fact that fracture will originate at the location that is most vulnerable in terms of flaw size and local variations in K_{Ic} , one might expect to observe some cases in which propagation into neighboring grains is governed by fracture energies lower than the polycrystalline values.

Most of the calculations involved integration along two or three branches of the single crystal crack velocity vs. K_I curve and two branches of the polycrystal curve. Region II of the polycrystal curves was assumed to extend to K_{Ic} where failure occurred.

In addition to the other assumptions, it was assumed that the ceramics were annealed before stressing. This assumption permits us to neglect the contribution that large scale residual stresses resulting from machining or other surface damage usually makes to the stress intensity factor (12,13).

Methods of numerical integration

The numerical integrations were done using a programmable printing calculator*.

The integrations involve several steps. A selected increment of time (ΔT) is used to calculate the applied stress (σ) using $\sigma = \sigma_0 + \dot{\sigma}\Delta T$ in which σ_0 is the stress applied in the previous step and $\dot{\sigma}$ is the stress rate. This is used to calculate K_I using

$$K_I = Y\sigma a^{1/2} \quad (3)$$

in which (a) is the crack size. Semi-circular surface flaws were assumed and Y was taken equal to 1.38 which is the value determined by Smith, Emery, and Kobayashi (14) for the highest K_I along the boundary of a semi-circular flaw. The new crack velocity is calculated using Equation (2). The crack velocity is used to increment the crack length using $a = a_0 + V\Delta T$ in which a_0 is the crack length from the previous step. Then, a new stress is calculated and the calculation is repeated. The computation stops when the desired value of K_I , a , σ , T , or V is reached.

Originally, the time increments were selected in advance. In many cases the original program was very inefficient because very small time increments were necessary to prevent overshooting the desired end point or overflowing the calculator. To remedy this problem a loop in the program is used to select an appropriate ΔT whenever the desired maximum increment of a particular variable such as K_I is exceeded. This change

* Hewlett Packard, Corvallis, Oregon, Model HP-97.

reduces the time necessary to integrate most curves with five branches to less than two hours.

Another precaution is that Equation (3) applies only for crack velocities less than the terminal crack velocity in a particular material (approximately $0.38 C_o$ where C_o is the longitudinal wave velocity in the material). The program compares the velocity calculated by Equation (3) with the terminal crack velocity and selects the lower value for calculation of the new crack length. Experience has shown that this precaution does not have an appreciable effect on the final results in most cases. In these calculations the terminal crack velocity of sapphire was taken as $3850 \text{ m} \cdot \text{s}^{-1}$.

The program was further revised making it possible to reverse the integration so that the initial flaw size could be estimated from the calculated critical flaw size. Comparison of calculated initial flaw sizes, determined using the fracture stresses and critical flaw sizes of fractured specimens, with the flaw sizes measured on the fracture surfaces, provided added assurance that the calculations were realistic. These calculations were made for five delayed fracture specimens and one specimen fractured using a constant loading rate. The specimens were 96% Al_2O_3 and were tested at 20% relative humidity. Although there is an error involved in using the values of n and A , determined for 40% humidity, to calculate the flaw sizes of specimens fractured at 20% humidity, this error is believed to be small. The magnitude of the error was estimated using earlier data (15) for the strengths of 96% alumina fractured at various humidities. The flaw sizes in specimens fractured at 20% relative humidity are about 10% smaller than those of specimens fractured at

40% relative humidity if comparison is made at the same probability of fracture.

In cases in which the crack growth began in a single crystal region and the critical crack boundary is in a polycrystalline region, the size of the flaw containing crystal must be known and the proper change in n and A made at this boundary. However, a preliminary calculation indicates that the likely errors in estimating the crystal size change the calculated initial flaw size only slightly. Also, in these cases, it is necessary to limit the crack velocity in the single crystal region to a maximum of the terminal crack velocity, otherwise the initial flaw sizes may have negative values.

III. Results

Constant stressing rate

Assuming 10 μm flaws in surface crystals of various sizes and a constant stressing rate of 10 MPas^{-1} , crack growth was calculated for coarse grained and fine grained alumina with the results shown in Figures 2 and 3. Although there is considerably less subcritical crack growth in the finer grained material with the lower K_{Ic} value, the amount of subcritical crack growth is still substantial with the critical crack lengths ranging from 400-1400% of the original flaw size depending on the size of the crystal containing the original flaw. In the coarser grained material the critical crack lengths ranged from 600-2800% of the original flaw size.

At a stressing rate of 10 MPas^{-1} , crystal sizes greater than 75 μm in the finer grained material and 100 μm in the coarser grained material were necessary before the crack would "go critical" with respect to the polycrystalline K_{Ic} in the flaw containing crystal, so that the crack was not slowed down noticeably at the crystal boundary.

Variable stressing rate

The results of the constant stressing rate calculations were used to select crystal sizes for variable stressing rate calculations for simulation of crack propagation at various stressing rates. The chosen crystal sizes were 50 μm and 100 μm . The stressing rates were chosen to indicate

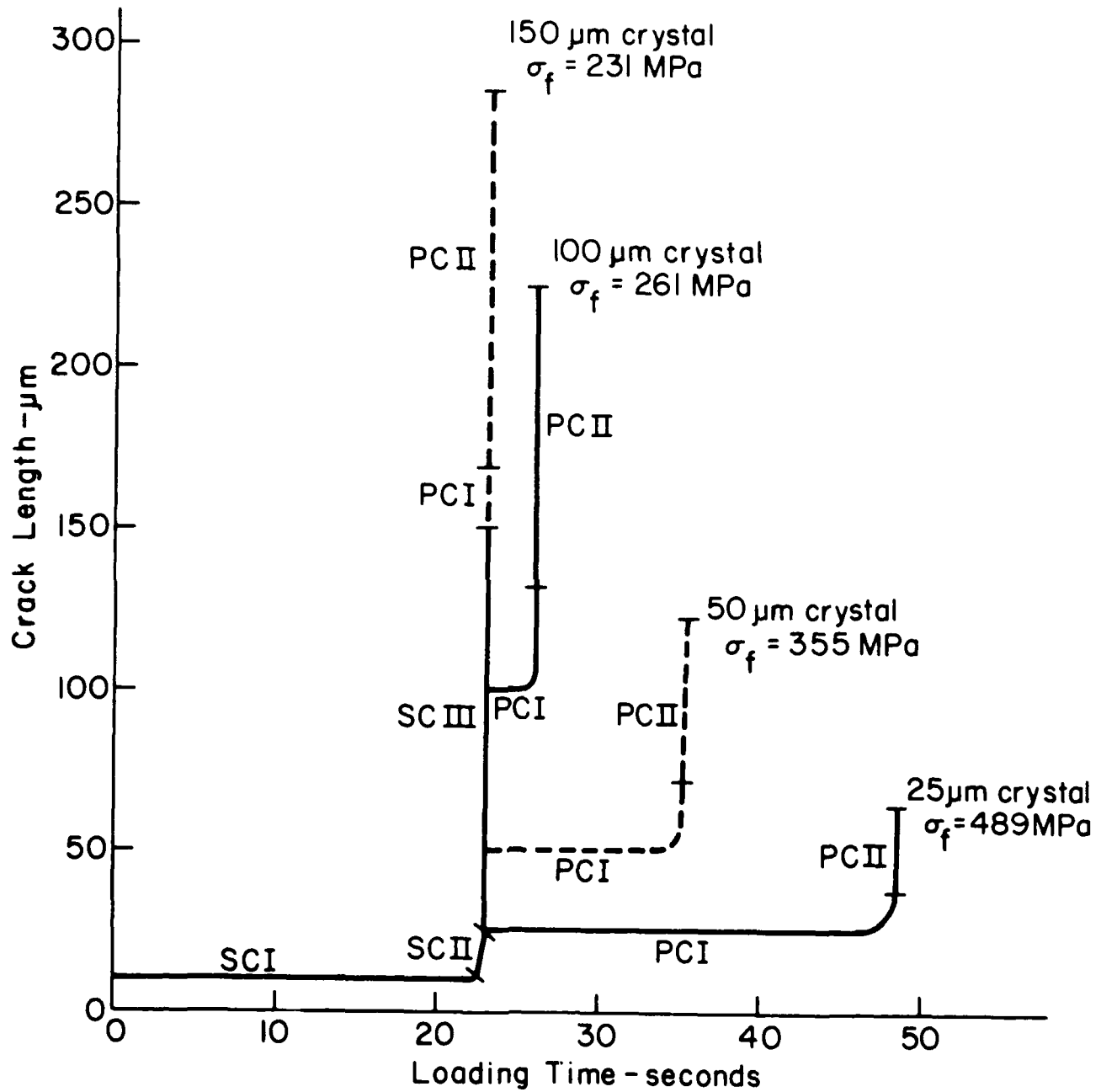


Figure 2 Crack length vs. time for 10 μm flaws in crystals of various sizes in a coarse grained alumina (10 MPa s^{-1} stressing rate, 50% relative humidity).

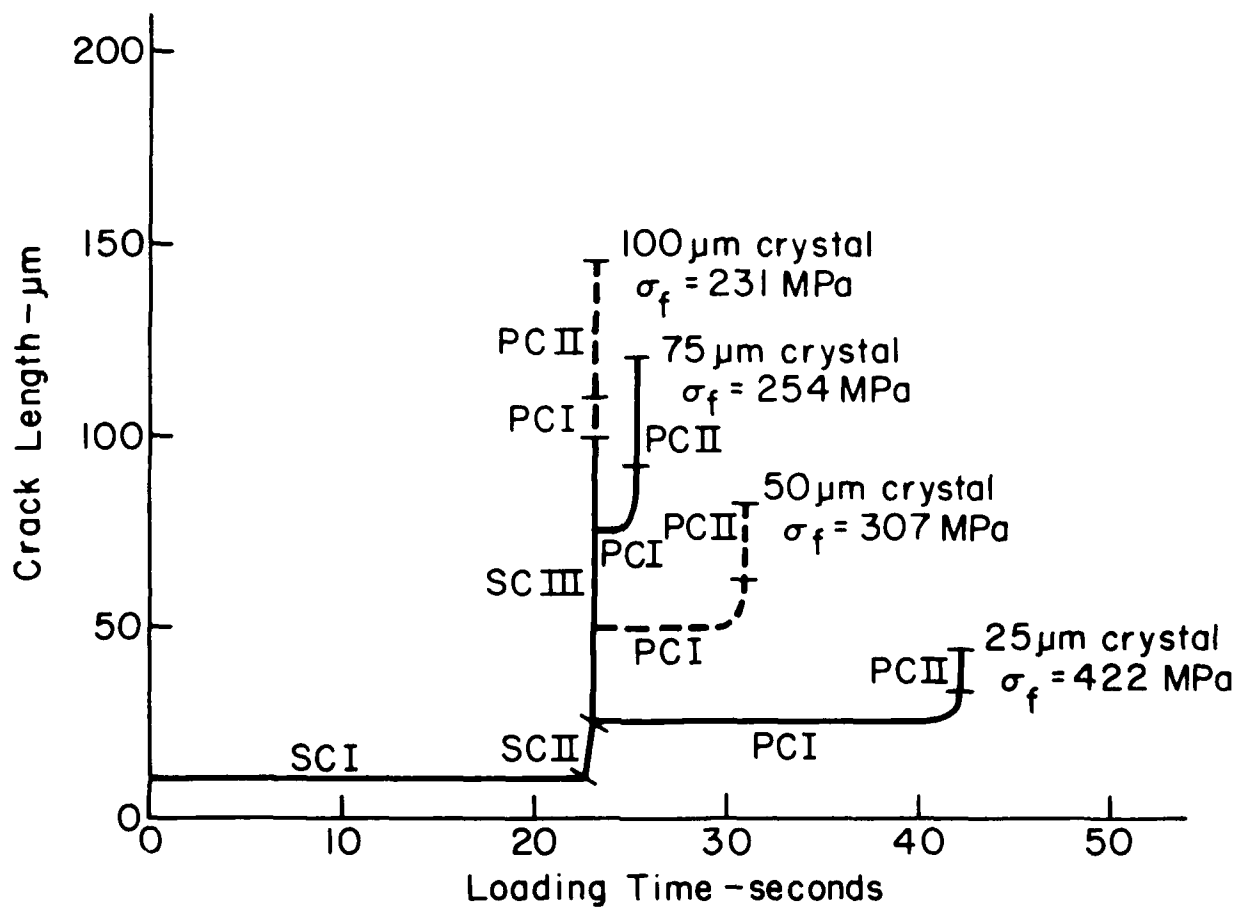


Figure 3 Crack length vs. time for 10 μm flaws in crystals of various sizes in a fine grained alumina (10 MPa s⁻¹ stressing rate, 50% relative humidity).

the range of stressing rates for which the crack behaved as though it was growing mainly in a medium with polycrystalline fracture properties and the range of stressing rates in which it behaved as though it was growing mainly in a medium with single crystal fracture properties. The results are given in Figures 4-7.

In the fine grained alumina with a 50 μm crystal at the fracture origin, stressing rates greater than 10^4 MPas^{-1} are necessary to suppress subcritical crack growth sufficiently so that K_I reached K_{Ic} before the crack reached the boundary of the 50 μm crystal. With a 100 μm crystal at the fracture origin, stressing rates greater than 10^2 MPas^{-1} were required. In this case, even at lower stressing rates, the rate of crack growth at the 100 μm crystal boundary is great enough so that the increases in K_I are caused mainly by increases in crack length so that there is little or no inflection of the a vs. K_I curves as they cross the boundary from single crystal to polycrystalline fracture properties.

In the coarse grained alumina with a 50 μm crystal at the fracture origin, the higher K_{Ic} of the polycrystalline material results in a greater range of stress intensity factors in which the crack is essentially arrested at the crystal boundary. Even at a stressing rate of 10^6 MPas^{-1} this range is substantial. Therefore, it appears that no reasonable stressing rate is sufficient to cause K_I to reach K_{Ic} before the crack reaches the boundary of the crystal. With a 100 μm crystal at the fracture origin, stressing rates greater than 10^4 MPas^{-1} were required.

Delayed fracture

To simulate delayed fracture tests, specimens with 10 μm flaws in 50 μm surface crystals were loaded at a constant stressing rate of 10^3

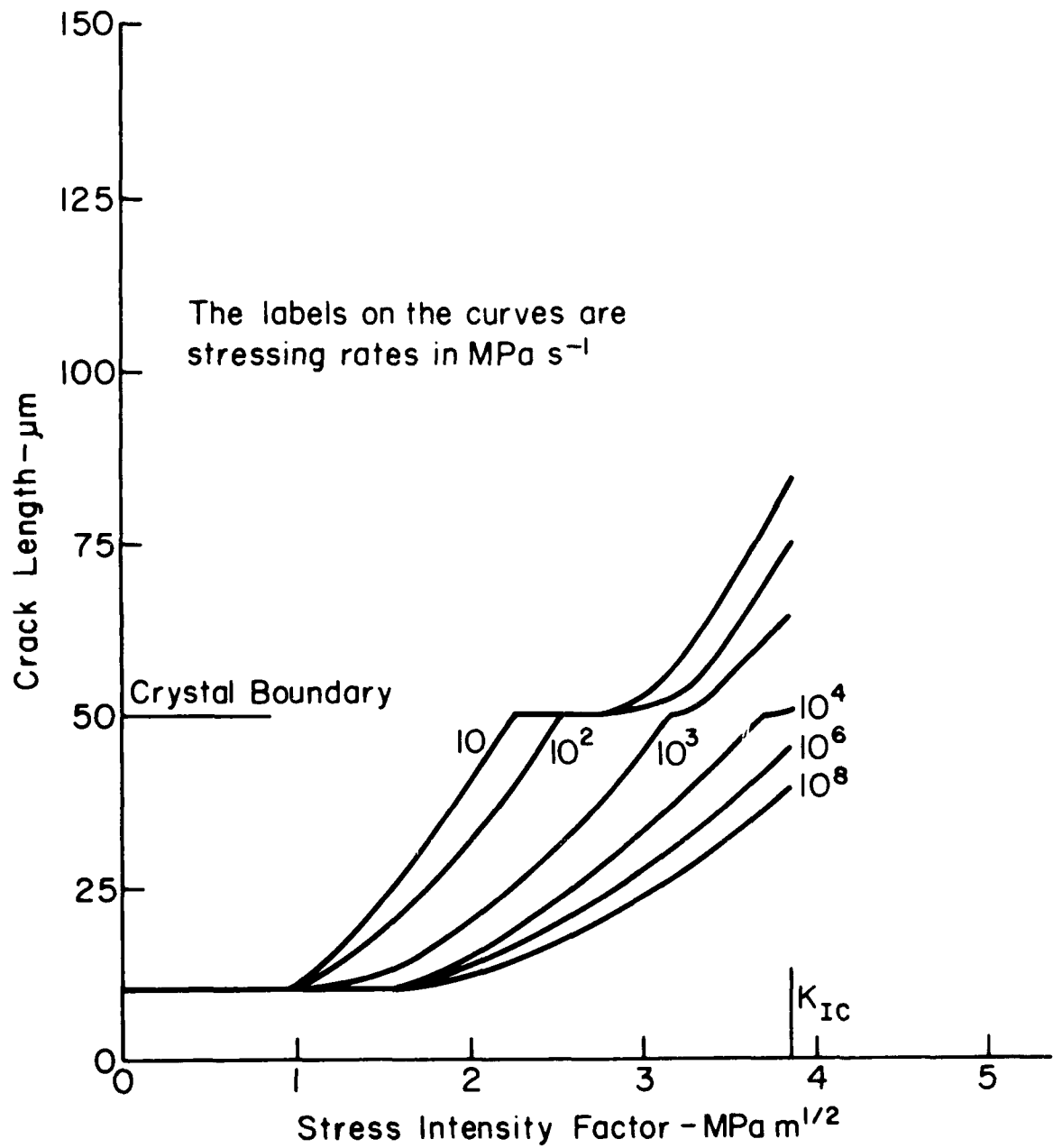


Figure 4 Crack length vs. stress intensity factor for various stressing rates in fine grained alumina; 10 μm flaw in a 50 μm crystal.

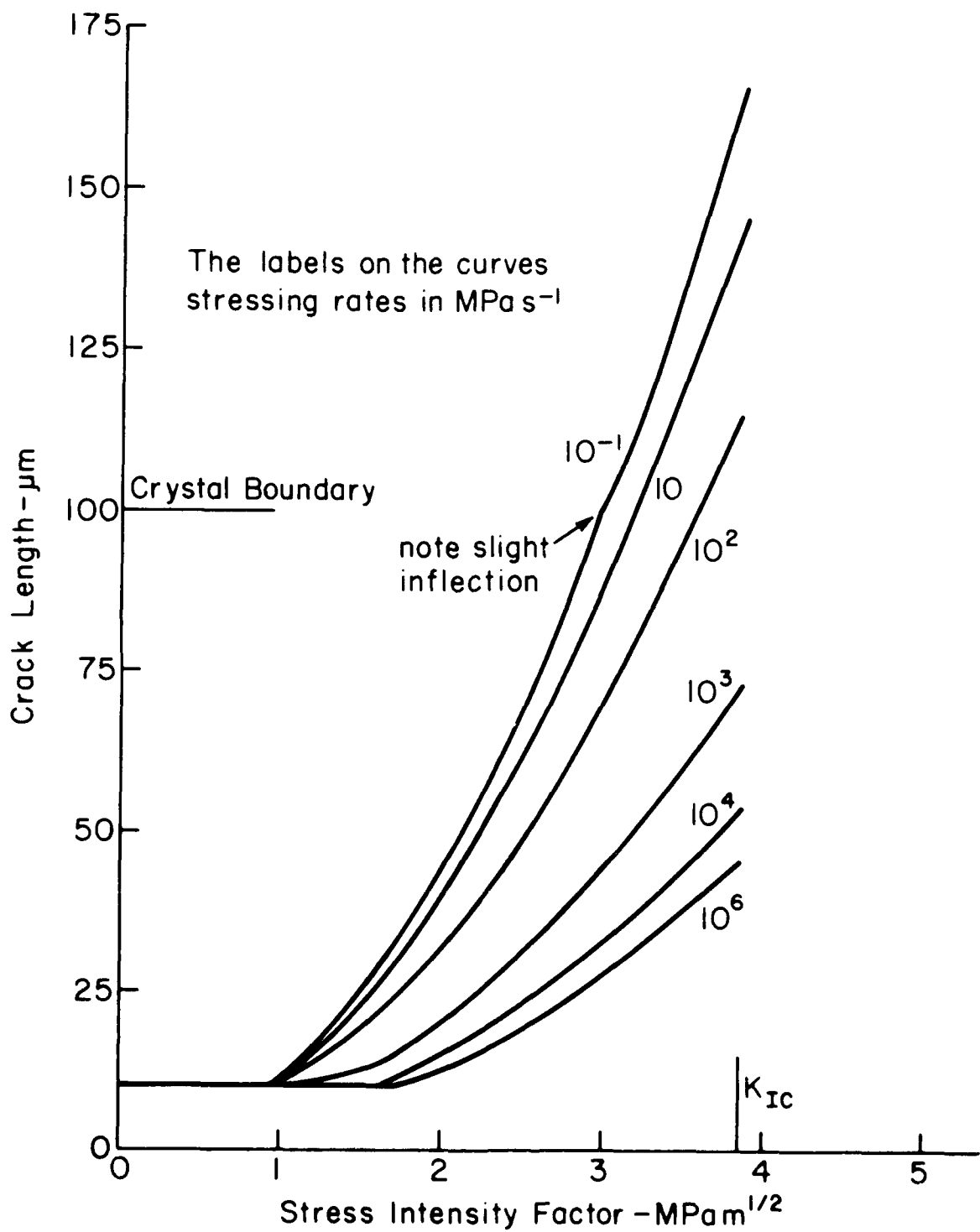


Figure 5 Crack length vs. stress intensity factor for various stressing rates in fine grained alumina; 10 μm flaw in a 100 μm crystal.

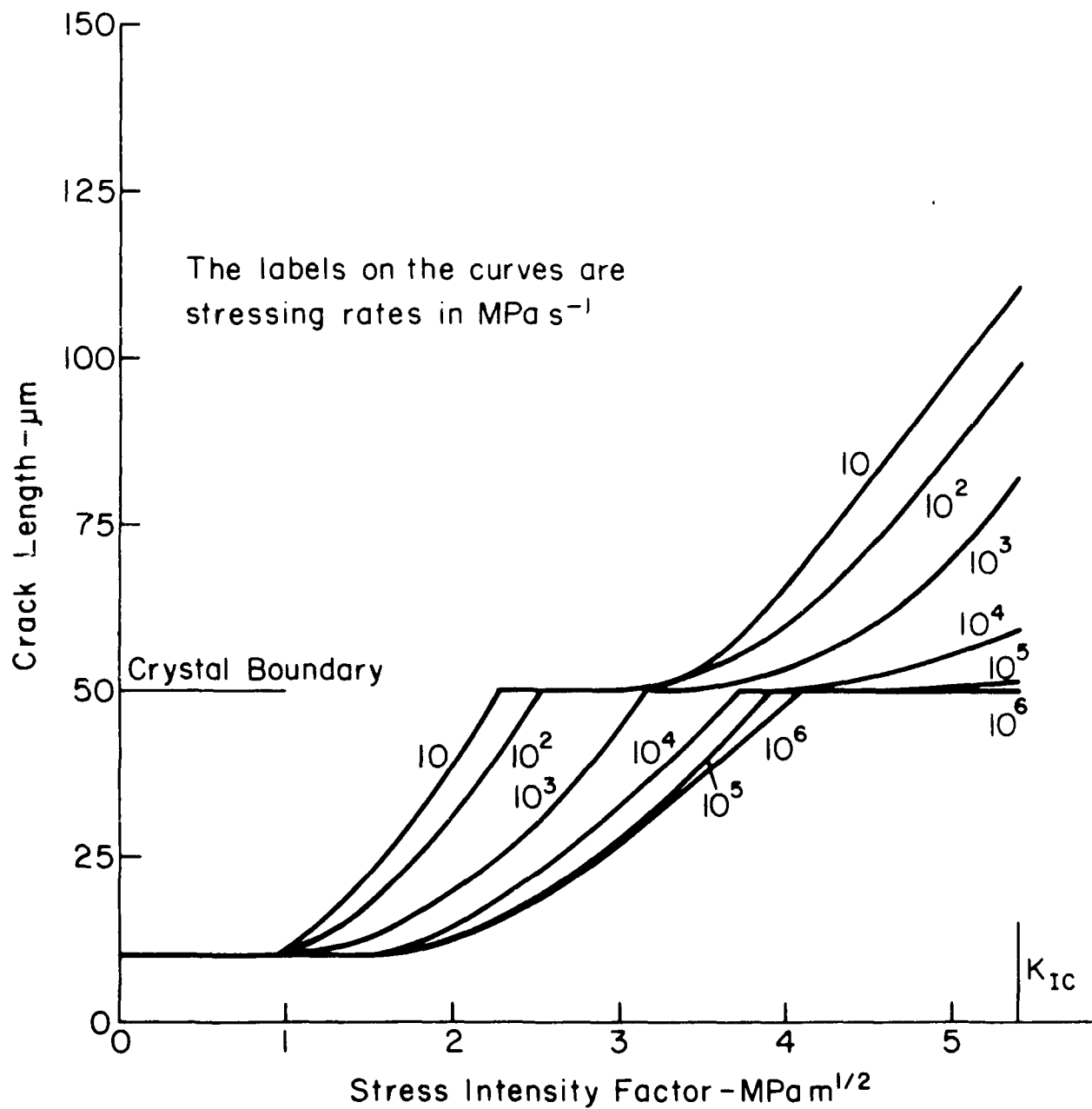


Figure 6 Crack length vs. stress intensity factor for various stressing rates in coarse grained alumina; $10\mu\text{m}$ flaw in a $50\mu\text{m}$ crystal.

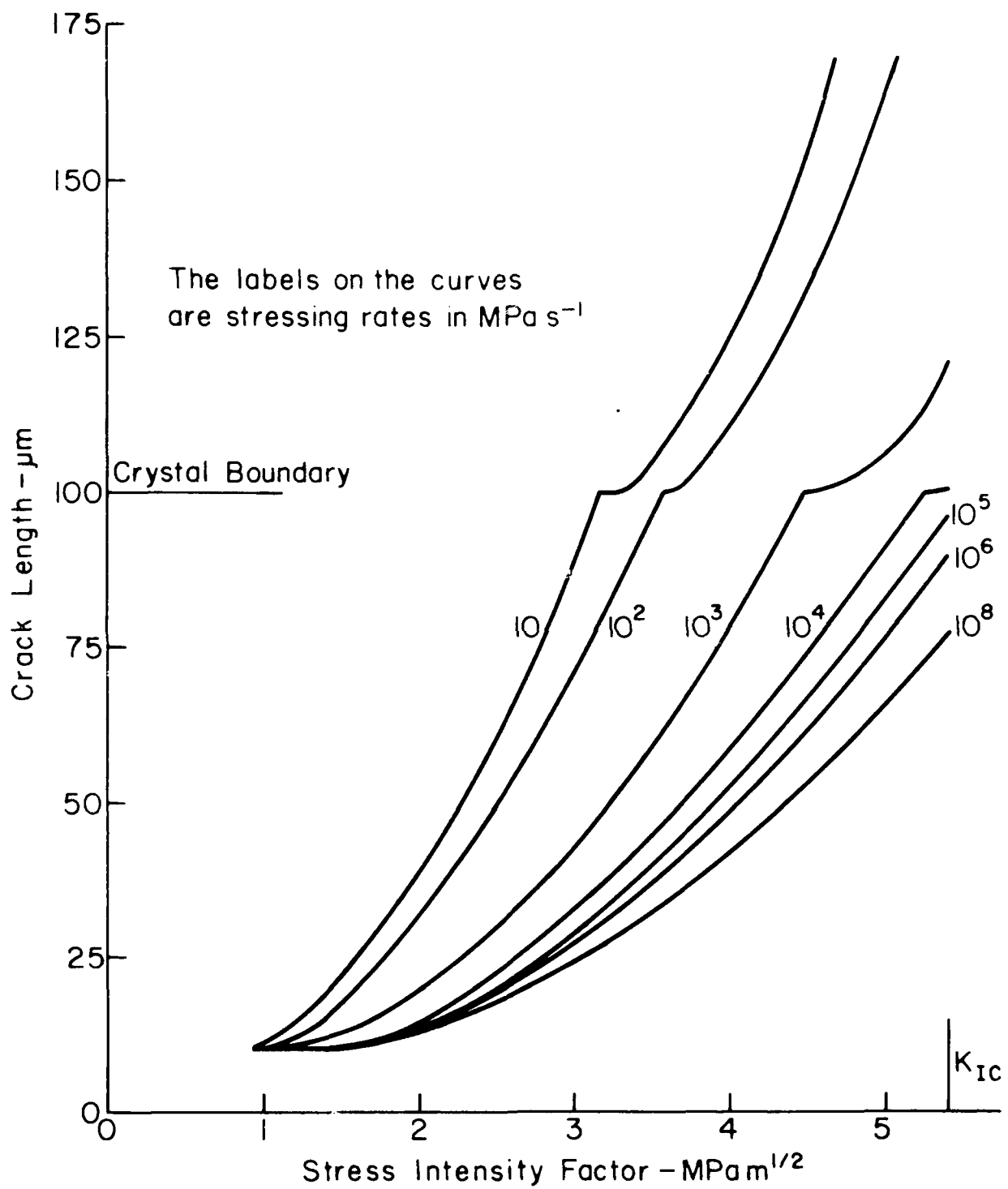


Figure 7 Crack length vs. stress intensity factor for various stressing rates in coarse grained alumina; 10 μm flaw in a 100 μm crystal.

Mas^{-1} until the desired stress was applied. This fairly high stressing rate was chosen to minimize the subcritical crack growth during loading and to assure that the loading time was a small fraction of the time to failure in most of the calculations. Then, the stress was held constant during subcritical crack growth and the time to failure was determined. The results are given in Figure 8 and are compared with results of similar calculations in which the flaw was assumed to extend to the boundary of the crystal when the loading began. The results show that over a wide range of times to failure there is no significant difference between the times to failure for the 10 μm flaws in the 50 μm crystals and the 50 μm flaws extending to the crystal boundaries. Evidently, the time required for the flaw to grow to the crystal boundary is negligible compared with the time to failure.

The delayed fracture curve for the fine grained alumina has a lower slope than that of the coarse grained alumina. As a result, at stresses less than about 225 MPa, the times to failure of the fine grained alumina are greater than those of the coarse grained body despite the much higher K_{Ic} of the coarse grained body. The shaded area in Figure 8 represents results of delayed fracture experiments using the fine grained 96% alumina. The upper limit is for the laboratory atmosphere and the lower limit is for a water environment. The fact that the calculated curve passes through this shaded area with an intermediate slope shows that the calculations are realistic. The 96% alumina used for these experiments was in the as-fired condition. This condition is consistent with the assumption of negligible large scale residual stresses at the surface flaws.

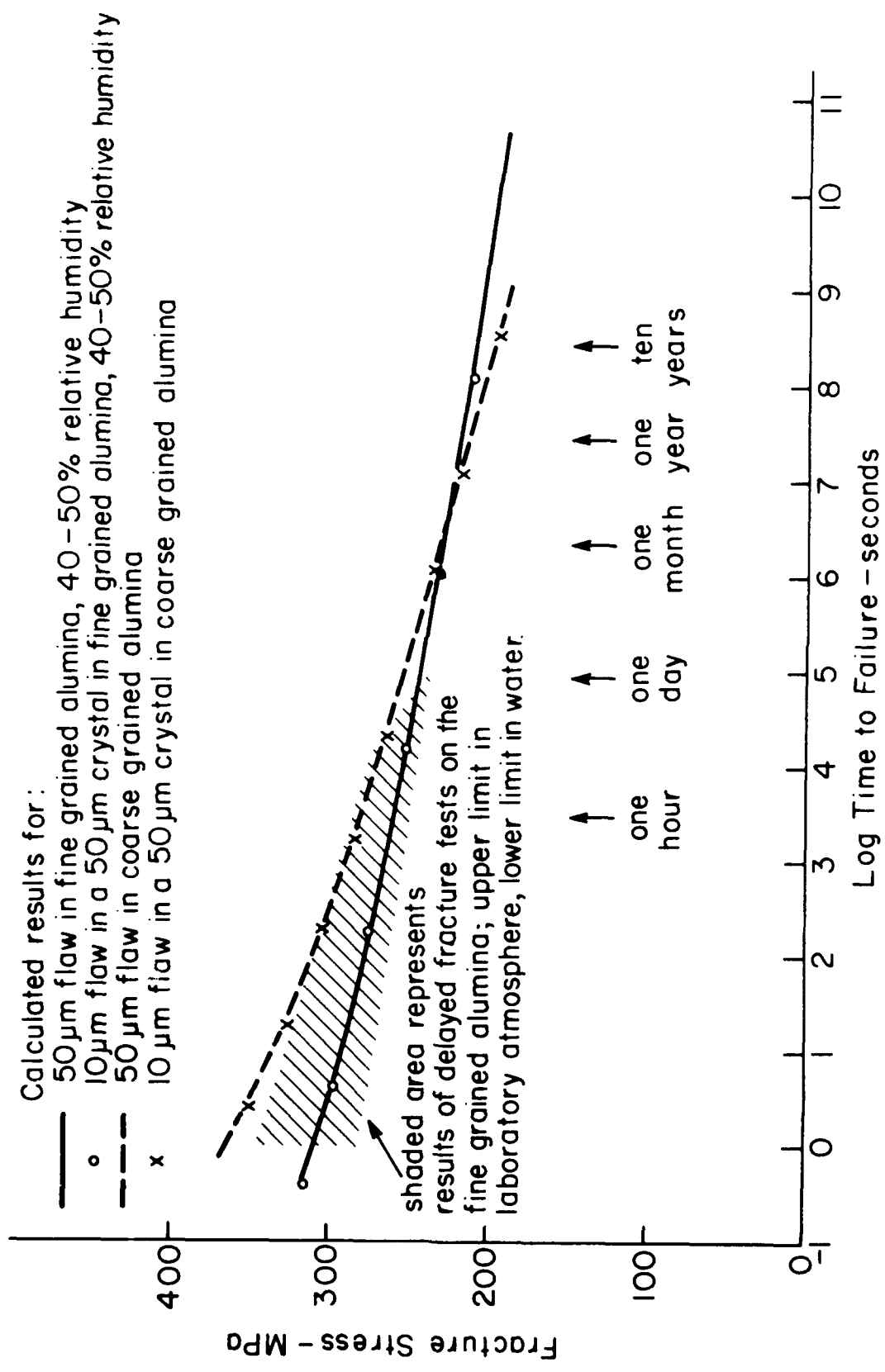


Figure 8 Fracture stress vs. log time for fine and coarse grained aluminas assuming either a 10 μm flaw in a 50 μm crystal or a 50 μm flaw in the polycrystalline body.

Comparison of calculated and measured values of initial flaw size

Critical flaw sizes in 96% alumina specimens, fractured in an earlier program (16,17) were calculated using Equation (1) in which semi-circular surface flaws were assumed and Y was taken as 1.27. Using these critical flaw sizes, the integrations were reversed to yield estimates of the initial flaw sizes. These flaw sizes were compared with the sizes of the flaws at the fracture origins, observed in scanning electron micrographs of the fracture surfaces. The results obtained for several delayed fracture specimens are given in Table II. Reasonable agreement between the calculated and measured values of initial flaw size was observed. The flaws in specimens D-3, D-11, and D-12 were stepped flaws whereas D-6 and D-7 were large crystals of 30 μm and 25 μm , respectively. In D-7 no flaw was visible in the large crystal so the entire crystal was assumed to be the flaw. In D-6, a small flaw was clearly visible at the surface of the crystal. In this case the calculation indicated that, at the crystal boundary, the crack growth rate drops from $3850 \text{ m}\cdot\text{s}^{-1}$ to $7.5 \cdot 10^{-8} \text{ m}\cdot\text{s}^{-1}$. The results obtained for specimen D-6 represent the best test of these crack growth estimates. In this case the original flaw size was 5 μm in a 30 μm crystal. The calculated critical flaw size was 51.1 μm , 1020% of the original flaw size, which is roughly in the middle of the range expected based on the constant stressing rate calculations.

In the case of a specimen fractured using a constant stressing rate, the calculated initial flaw size was 28.6 μm . This flaw size is in reasonable agreement with the size of the large crystal (20 μm) observed at the

TABLE II

Comparison of Calculated and Measured Values of
Initial Flaw Size of Delayed Fracture Specimens

Specimen No.	Fracture Stress MPa	Critical Flaw Size μm	Initial Flaw Size Observed μm	Initial Flaw Size Calculated μm	Time to Failure s
D-3	352	73.8	40	38.5	22
D-6	400	51.1	5*	3.3*	51
D-7	333	82.5	25**	41.1**	77
D-11	362	69.8	25-35	32.9	232
D-12	384	62.0	30	28.3	453

*Flaw in a large crystal.

**Large crystal fracture origin.

fracture origin. The stressing rate used in this calculation was based on the assumption that failure occurred in one minute.

The results in this section show that the calculations yield reasonable estimates of the initial flaw sizes and that it is unlikely that these fractures are controlled by single crystal fracture energies even in the case in which fracture originated at a 5 μm flaw in a 30 μm crystal.

IV. Discussion and Conclusions

A basic assumption on which these calculations are based is that when the crack passes the crystal boundary, the crack velocity will immediately or almost immediately change to that expected based on the polycrystalline V vs. K_I curve. The energy acquired by the crack while it is in the crystal, in excess of that required for crack propagation in the crystal, depends on the elastic energy input to the crack and is partitioned among the stress wave energy (5), the excess surface energy absorbed by K_I dependent mechanisms, and the kinetic energy. Clark and Irwin (18) refer to running cracks as low-inertia disturbances that cannot be driven faster than about half of the elastic shear wave velocity. Therefore, it is reasonable to assume that the kinetic energy is small and has a definite upper limit depending on the shear wave velocity. Conservation of energy requires that, after the crack crosses the crystal boundary into the polycrystalline region, the energy required to make up the difference between the elastic energy input and the fracture energy absorbed in this region which requires much greater fracture energy for propagation, must be drawn from the kinetic energy.

Quantitative methods are not available to permit determination of the kinetic energy. However, it is possible to estimate an upper limit to crack propagation before "arrest" in the polycrystalline region by equating the excess elastic energy supplied to the crack tip while it is in the crystal to the excess fracture energy absorbed in the polycrystalline region. This calculation requires integration over the area of crack growth

in each case. This was done for the case of a crack that went critical at a crack radius of 25 μm in a 50 μm crystal. At a radius of 56 μm , the excess elastic energy had been entirely absorbed as fracture energy. These results show that it is reasonable to assume that the crack slows down to the crack velocity expected based on the polycrystalline V vs. K_I curve as the crack passes the crystal boundary.

The results of the crack growth calculations show that, in alumina ceramics with small flaws in large grains, there is a range of flaw sizes, grain sizes, and stressing rates in which the crack growth becomes critical with respect to the polycrystalline K_{Ic} before the crack reaches the boundary of the grain in which the fracture originates. However, in the cases examined thus far, substantial subcritical crack growth occurred, significantly changing the critical flaw size and fracture stress. This was true, even at very high stressing rates. This finding is in basic disagreement with the assumption of Rice and co-workers that subcritical crack growth can be neglected so that fracture energies can be calculated from initial flaw sizes at fracture origins and the fracture stresses.

The effects of neglecting subcritical crack growth on fracture energies are indicated in Figure 9. The calculated fracture energies are called apparent fracture energies. As indicated by the solid line in the figure, the apparent fracture energies, calculated based on the original flaw size and assuming that the crack propagation is controlled by the polycrystalline properties (A and n), are lower than polycrystalline fracture energies but not drastically so. However, in cases in which subcritical crack growth occurs in relatively large single crystals at the fracture

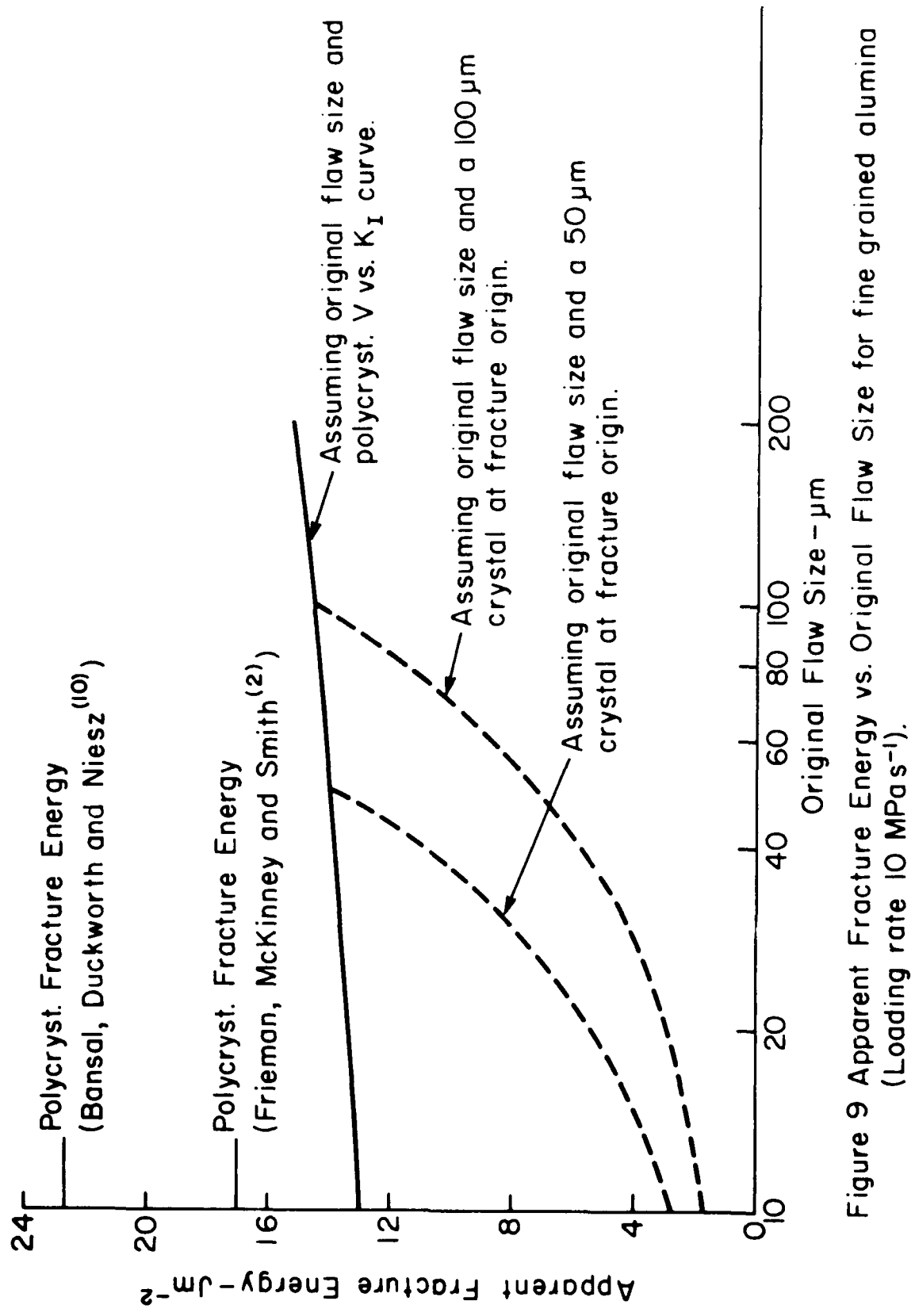


Figure 9 Apparent Fracture Energy vs. Original Flaw Size for fine grained alumina (Loading rate $10\ \text{MPa s}^{-1}$).

origins (indicated by the dashed lines for 50 and 100 μm crystals) there is a drastic reduction in the apparent fracture energy. This reduction is caused by the extensive subcritical crack growth that occurs in these cases which reduces the calculated fracture stresses. These low fracture stresses, when combined with the underestimated flaw sizes that result from using the original flaw sizes instead of the critical flaw sizes, yield substantial underestimates of the fracture energies.

The present method of calculation can be used to investigate the probability that fractures in alumina will be controlled by the single crystal K_{Ic} in practical applications. It seems clear that most practical applications involve static loads or low stressing rates. As indicated by the delayed fracture simulations, it is unlikely that, under these conditions, the fractures will be controlled by the single crystal K_{Ic} . In fractures occurring at high loading rates (ceramic armor, impacts of pellets on high intensity lighting envelopes or electrical insulation, interrupted cutting with ceramic cutting tools, etc.), control by the single crystal K_{Ic} is more likely. Kirchner, Gruver, and Sotter (16,17) characterized flaws at fracture origins in 96% alumina and H. P. alumina for various loading rates and temperatures. Depending on the conditions, the percentage of fractures originating at large crystals ranged from 0 to 65% but frequently was about 20-30%. These crystals were less than 50 μm in size with possible rare exceptions. Therefore, present evidence indicates that in fractures originating at large crystals, the polycrystalline K_{Ic} will control fracture in most cases and that the single crystal K_{Ic} will control fracture only in the case of the largest crystals and the highest loading rates.

Further thought should be given to several other effects including:

1. The effect of residual stresses at the machining flaws.
2. The possible effect of localized variations in preferred orientation on localized K_{Ic} .

Residual stresses can have a profound effect on the K_I values actually present at crack tips. Petrovic et al. (12) found that residual stresses at Vickers indentations in H.P. Si_2N_4 reduced measured K_{Ic} to about 3.5 MPam^{1/2} from the value of 4.7 MPam^{1/2} otherwise expected. Kirchner and Isaacson (13) found a similar reduction in the case of single point diamond grinding damage where measured K_{Ic} values were reduced to about 2.8 MPam^{1/2}. In addition, stresses caused by thermal expansion anisotropy may have a more localized effect. If these effects are as large in alumina as in H.P. Si_3N_4 , it seems possible that in some cases the original flaws might propagate to the grain boundary under the influence of the residual stresses alone.

The presence of preferred orientation will probably result in a gradual transition from single crystal to polycrystalline fracture energies near the crystal boundary. In evaluating this possibility it is well to remember that, in effect, the fracture seeks out the most vulnerable fracture origin in terms of flaw size and severity, susceptibility to subcritical crack growth and local K_{Ic} . Thus, if there are two similar flaws in two similar crystals but one is surrounded by a region of preferred orientation that is favorable for subcritical crack growth and the other is surrounded by randomly oriented crystals the resulting fracture

surface will contain the flaw surrounded by the region of preferred orientation and will not contain the other flaws.

It cannot be emphasized too strongly that, in polycrystalline ceramics, fracture depends on the flaw size and severity, the resistance to subcritical crack growth and the K_{Ic} , not just on K_{Ic} alone. The single crystal K_{Ic} values are most likely to control fracture in cases in which the flaw is small or blunt, there is substantial resistance to subcritical crack growth and the single crystal K_{Ic} is not much less than the polycrystalline K_{Ic} .

Acknowledgements

The authors are pleased to acknowledge the contributions of their associates at Ceramic Finishing Company including D. M. Richard who developed the original calculator program and J. V. Firchner who made revisions to the program including insertion of the variable time base, and the sponsorship of the Office of Naval Research.

References

1. R. W. Rice, "Fractographic Identification of Strength-Size Relations, Flaws, and Microstructure," from Fracture Mechanics of Ceramics, Vol. 1, Edited by R. C. Bradt, D. P. H. Hasselman, and F. J. Lange, Plenum, New York (1974), pages 373-393.
2. J. J. Irwin, R. R. McKinney, and H. L. Smith, "Slow Crack Growth in Polycrystalline Ceramics," from Fracture Mechanics of Ceramics, Vol. 1, Edited by R. C. Bradt, D. P. H. Hasselman, and F. J. Lange, Plenum, New York (1974), pages 67-76.
3. S. W. Freiman, L. J. Mecholsky, Jr., and P. A. Rice, "Influence of Microstructure on Crack Propagation in Oxide," J. Amer. Ceram. Soc., 53 (10) 4964-4971 (1970).
4. R. W. Rice, S. W. Freiman, L. J. Mecholsky, and R. R. McKinney, "Effect of Flaw: Grain-Size Ratio on Fracture Energy," Paper 348-75, Annual Meeting of the American Ceramic Society, Bull. Amer. Ceram. Soc., 55 (4) 395 (1976).
5. J. P. Singh, A. V. Virkar, D. K. Shetty, and R. S. Berlin, "Strength-Grain Size Relations in Polycrystalline Ceramics," J. Amer. Ceram. Soc., 62 (3-4) 179-183 (1979).
6. H. P. Kirchner, unpublished research (1979).
7. S. M. Wiederhorn, "Moisture Assisted Crack Growth in Ceramics," J. of Fracture Mechanics 4 (2) 171-177 (1968).
8. S. M. Wiederhorn, "Subcritical Crack Growth in Ceramics," from Fracture Mechanics of Ceramics, Vol. 1, Edited by R. C. Bradt, D. P. H. Hasselman, and F. J. Lange, Plenum, New York (1974), pages 11-20.
9. A. G. Evans, "A Method for Evaluating the Size-Dependent Strength of Brittle Materials - and Its Application to Polycrystalline Alumina," J. Mater. Sci., 7, 1135-1147 (1972).
10. R. W. Davidge and G. Taplin, "The Effective Surface Energy of Brittle Materials," J. Mater. Sci., 9, 165-177 (1969).
11. G. K. Bansal, W. H. Duckworth, and A. G. Evans, "Strength-Size Relations in Ceramic Materials: Investigation of an Alumina Ceramic," J. Amer. Ceram. Soc., 62 (10-11) 1774-1781 (1979).
12. J. P. Dutromy, J. A. Desrosiers, J. R. Lavoie, and G. Tremblay, "Effect of Surface Oxidation on the Strength of Ceramics," J. Amer. Ceram. Soc., 62 (10-11) 1766-1773 (1979).

AD-A085 874 CERAMIC FINISHING CO STATE COLLEGE PA F/8 11/2
LOCALIZED IMPACT DAMAGE IN CERAMICS. LOCALIZED IMPACT DAMAGE TN--ETC(1)
FEB 80 H P KIRCHNER, T J LARCHUK, J M RAGOSTA N00014-74-C-0241
NL

UNCLASSIFIED

2 OF 2
20
20
20

END
DATE
FILED
8-80
DTIC

13. H. P. Kirchner and E. A. Isaacson, "Material Removal and Damage Penetration During Abrasive Machining of Ceramics," Ceramic Finishing Company, Third Quarterly Report, Contract DAR78-18097 (December, 1979).
14. F. W. Smith, A. F. Emery, and A. S. Kobayashi, "Stress Intensity Factors for Semi-Circular Cracks, Part II - Semi-Infinite Solid," *J. Appl. Mech.* 34, Series E, 953-956 (December, 1967).
15. H. P. Kirchner, R. M. Gruver, and R. E. Walker, "Strength Effects Resulting from Simple Surface Treatments," from *The Science of Ceramic Machining and Surface Finishing*, Edited by S. J. Schneider, Jr. and R. W. Rice, NBS Special Publication 348 (1972), pages 353-363.
16. H. P. Kirchner, R. M. Gruver, and W. A. Sotter, "Characteristics of Flaws at Fracture Origins and Fracture Stress-Flaw Size Relations in Various Ceramics," *Mater. Sci. Eng.* 22, 147-156 (1976).
17. R. M. Gruver, W. A. Sotter, and H. P. Kirchner, "Variation of Fracture Stress with Flaw Character in 96% Al_2O_3 ," *Amer. Ceram. Soc. Bull.* 55 (2) 198-202 (1976).

BASIC DISTRIBUTION LIST

Technical and Summary Reports		No. of Copies	
<u>Organization</u>	No. of Copies		<u>Organization</u>
Defense Documentation Center Cameron Station Alexandria, Virginia 22314	(12)	Naval Construction Battalion Civil Engineering Laboratory Port Hueneme, California 93043 Attn: Materials Division	(1)
Office of Naval Research Department of the Navy Arlington, Virginia 22217 Attn: Code 471 Code 102 Code 470	(1) (1) (1)	Naval Electronics Laboratory Center San Diego, California 92152 Attn: Electron Materials Sciences Division	(1)
Commanding Officer Office of Naval Research Branch Office 495 Summer Street Boston, Massachusetts 02210	(1)	Naval Missile Center Materials Consultant Code 3312-1 Point Mugu, California 93041	(1)
Commanding Officer Office of Naval Research Branch Office 536 South Clark Street Chicago, Illinois 60605	(1)	Commanding Officer Naval Surface Weapons Center White Oak Laboratory Silver Spring, Maryland 20910 Attn: Library	(1)
Office of Naval Research San Francisco Area Office 760 Market Street, Room 447 San Francisco, California 94102	(1)	David W. Taylor Naval Ship R&D Center Materials Department Annapolis, Maryland 21402	(1)
Naval Research Laboratory Washington, D.C. 20390		Naval Undersea Center San Diego, California 92132 Attn: Library	(1)
Attn: Code 6000 Code 6100 Code 6300 Code 6400 Code 2627	(1) (1) (1) (1) (1)	Naval Underwater System Center Newport, Rhode Island 02840 Attn: Library	(1)
Naval Air Development Center Code 302 Warminster, Pennsylvania 18974 Attn: Mr. F. S. Williams	(1)	Naval Weapons Center China Lake, California 93555 Attn: Library	(1)
Naval Air Propulsion Test Center Trenton, New Jersey 08628 Attn: Library	(1)	Naval Postgraduate School Monterey, California 93940 Attn: Mechanical Engineering Dept.	(1)
		Naval Air Systems Command Washington, D.C. 20360	
		Attn: Code 52031 Code 52032 Code 320	(1) (1) (1)

BASIC DISTRIBUTION LIST (Cont'd)

<u>Organization</u>	<u>No. of Copies</u>	<u>Organization</u>	<u>No. of Copies</u>
Naval Sea System Command Washington, D.C. 20362 Attn: Code 035	(1)	NASA Headquarters Washington, D.C. 20546 Attn: Code RRM	(1)
Naval Facilities Engineering Command Alexandria, Virginia 22331 Attn: Code 03	(1)	NASA Lewis Research Center 21000 Brookpark Road Cleveland, Ohio 44135 Attn: Library	(1)
Scientific Advisor Commandant of the Marine Corps Washington, D.C. 20380 Attn: Code AX	(1)	National Bureau of Standards Washington, D.C. 20234 Attn: Metallurgy Division Inorganic Materials Division	(1)
Naval Ship Engineering Center Department of the Navy CTR BG #2 3700 East-West Highway Prince Georges Plaza Hyattsville, Maryland 20782 Attn: Engineering Materials and Services Office, Code 6101	(1)	Defense Metals and Ceramics Information Center Battelle Memorial Institute 505 King Avenue Columbus, Ohio 43201	(1)
Army Research Office Box CM, Duke Station Durham, North Carolina 27706 Attn: Metallurgy & Ceramics Div.	(1)	Director Ordnance Research Laboratory P.O. Box 30 State College, Pennsylvania 16801	(1)
Army Materials and Mechanics Research Center Watertown, Massachusetts 02172 Attn: Res. Programs Office (AMOMR-P)	(1)	Director Applied Physics Laboratory University of Washington 1013 Northeast Fortieth Street Seattle, Washington 98105	(1)
Air Force Office of Scientific Research Bldg. 410 Bolling Air Force Base Washington, D.C. 20332 Attn: Chemical Science Directorate Electronics and Solid State Sciences Directorate	(1)	Metals and Ceramics Division Oak Ridge National Laboratory P.O. Box X Oak Ridge, Tennessee 37380	(1)
Air Force Materials Lab (LA) Wright-Patterson AFB Dayton, Ohio 45433	(1)	Los Alamos Scientific Laboratory P.O. Box 1663 Los Alamos, New Mexico 87544 Attn: Report Librarian	(1)
		Argonne National Laboratory Metallurgy Division P.O. Box 229 Lemont, Illinois 60439	(1)

BASIC DISTRIBUTION LIST (Cont'd)

<u>Organization</u>	<u>No. of Copies</u>	<u>Organization</u>	<u>No. of Copies</u>
Brookhaven National Laboratory Technical Information Division Upton, Long Island New York 11973 Attn: Research Library	(1)	Dr. G. Schmidt Air Force Materials Laboratory Wright-Patterson AFB Dayton, OH 54533	(1)
Library Building 50 Room 134 Lawrence Radiation Laboratory Berkeley, California	(1)	Dr. D. A. Shockey Stanford Research Institute Poulter Laboratory Menlo Park, CA 94025	(1)
Dr. J. D. Buch Prototype Development Assoc., Inc. 1740 Garry Avenue, Suite 201 Santa Ana, CA 92705	(1)	Mr. T. Derkus TRW Cleveland, OH 44117	(1)
Dr. B. Budiansky Harvard University Department of Engineering and Applied Science Cambridge, MA 02138	(1)	Dr. S. Hart Naval Research Laboratory Washington, DC 20375	(1)
Professor H. Conrad University of Kentucky Materials Department Lexington, KY 40506	(1)	Professor G. Kino Stanford University Palo Alto, CA 94305	(1)
Dr. A. Cooper Case Western Reserve University Materials Department Cleveland, OH 44106	(1)	Dr. J. Krumhansl Physics Department Cornell University Ithica, NY 14850	(1)
Dr. I. Finney University of California Berkeley, CA 94720	(1)	Dr. R. E. Loehman University of Florida Ceramics Division Gainesville, FL 32601	(1)
Mr. A. A. Fyall Royal Aircraft Establishment Farnborough, Hants UNITED KINGDOM	(1)	Dr. D. Mulville Office of Naval Research Code 474 800 North Quincy Street Arlington, VA 22217	(1)
Dr. R. Jaffee Electric Power Research Institute Palo Alto, CA	(1)	Dr. N. Perrone Office of Naval Research Code 474 800 North Quincy Street Arlington, VA 22217	(1)
Dr. L. Rubin Aerospace Corporation P.O. Box 92957 Los Angeles, CA 90009	(1)	Dr. J. R. Rice Brown University Division of Engineering Providence, RI 02912	(1)

SUPPLEMENTARY DISTRIBUTION LIST

Technical and Summary Reports

<u>Organization</u>	<u>No. of Copies</u>	<u>Organization</u>	<u>No. of Copies</u>
Dr. W.F. Adler Effects Technology Inc. 5383 Hollister Avenue P.O. Box 30400 Santa Barbara, CA 92105	(1)	Professor A.H. Heuer Case Western Reserve University University Circle Cleveland, OH 44106	(1)
Dr. G. Bansal Battelle 505 King Avenue Columbus, OH 43201	(1)	Dr. R. Hoagland Battelle 505 King Avenue Columbus, OH 43201	(1)
Dr. R. Bratton Westinghouse Research Lab. Pittsburgh, PA 15235	(1)	Dr. R. Jaffee Electric Power Research Institute Palo Alto, CA	(1)
Dr. A.G. Evans Rockwell International P.O. Box 1085 1049 Camino Dos Rios Thousand Oaks, CA 91360	(1)	Dr. P. Jorgensen Stanford Research Institute Poulter Laboratory Menlo Park, CA 94025	(1)
Mr. E. Fisher Ford Motor Co. Dearborn, MI	(1)	Dr. R.N. Katz Army Materials and Mechanics Research Center Watertown, MA 02171	(1)
Dr. P. Gielisse University of Rhode Island Kingston, RI 02881	(1)	Dr. H. Kirchner Ceramic Finishing Company P.O. Box 498 State College, PA 16801	(1)
Dr. M.E. Gulden International Harvester Company Solar Division 2200 Pacific Highway San Diego, CA 92138	(1)	Dr. B. Koepke Honeywell, Inc. Corporate Research Center 500 Washington Avenue, South Hopkins, MN 55343	(1)
Dr. D.P.H. Hasselman Montana Energy and MHD Research and Development Institute P.O. Box 3809 Butte, Montana 59701	(1)	Mr. Frank Koubek Naval Surface Weapons Center White Oak Laboratory Silver Spring, MD 20910	(1)
Mr. G. Hayes Naval Weapons Center China Lake, CA 93555	(1)	E. Krafft Carborundum Co. Niagara Falls, NY	(1)

SUPPLEMENTARY DISTRIBUTION LIST (Cont'd)

<u>Organization</u>	<u>No. of Copies</u>	<u>Organization</u>	<u>No. of Copies</u>
Dr. S.A. Bortz IITRI 10 W. 35th Street Chicago, IL 60616	(1)	Major W. Simmons Air Force Office of Scientific Research Building 410 Bolling Air Force Base Washington, DC 20332	(1)
Mr. G. Schmitt Air Force Materials Laboratory Wright-Patterson AFB Dayton, OH 45433	(1)	Dr. P. Becher Naval Research Laboratory Code 6362 Washington, DC 20375	(1)
Dr. Stan Wolf Division of Materials and Science Department of Energy Washington, DC 20545	(1)	Mr. L.B. Weckesser Applied Physics Laboratory Johns Hopkins Road Laurel, MD 20810	(1)
Dr. W.G.D. Frederick Air Force Materials Laboratory Wright-Patterson AFB Dayton, OH 45433	(1)	Mr. D. Richardson AiResearch Manufacturing Company 4023 36th Street P.O. Box 5217 Phoenix, AZ 85010	(1)
Dr. P. Land Air Force Materials Laboratory Wright-Patterson AFB Dayton, OH 45433	(1)	Dr. H.E. Bennett Naval Weapons Center Code 3818 China Lake, CA 93555	(1)
Mr. K. Letson Redstone Arsenal Huntsville, AL 35809	(1)	Mr. G. Denman Air Force Materials Laboratory Code LPJ Wright-Patterson AFB Dayton, OH 45433	(1)
Dr. S. Freiman Naval Research Laboratory Code 6363 Washington, DC 20375	(1)	Dr. D. Godfrey Admiralty Materials Laboratory Polle, Dorset BH16 6JU UNITED KINGDOM	(1)
Director Materials Sciences Defense Advanced Research Projects Agency 1400 Wilson Boulevard Arlington, VA 22209	(1)	Dr. N. Corney Ministry of Defense The Adelphi John Adam Street London WC2N 6BB UNITED KINGDOM	(1)
Dr. James Pappis Raytheon Company Research Division 28 Sycamore Street Waltham, MA 02154	(1)		

SUPPLEMENTARY DISTRIBUTION LIST (Cont'd)

<u>Organization</u>	<u>No. of Copies</u>	<u>Organization</u>	<u>No. of Copies</u>
Dr. F.F. Lange Rockwell International P.O. Box 1085 1049 Camino Dos Rios Thousand Oaks, CA 91360	(1)	Dr. J. Ritter University of Massachusetts Department of Mechanical Engineering Amherst, MA 01002	(1)
Dr. J. Lankford Southwest Research Institute 8500 Culebra Road San Antonio, TX 78284	(1)	Professor R. Roy Pennsylvania State University Materials Research Laboratory University Park, PA 16802	(1)
Library Norton Company Industrial Ceramics Division Worcester, MA 01606	(1)	Dr. R. Ruh AFML Wright-Patterson AFB Dayton, OH 45433	(1)
State University of New York College of Ceramics at Alfred University Attn: Library Alfred, NY 14802	(1)	Mr. J. Schuldies AiResearch Phoenix, AZ	(1)
Dr. L. Hench University of Florida Ceramics Division Gainesville, FL 32601	(1)	Professor G. Sines University of California, Los Angeles Los Angeles, CA 90024	(1)
Dr. N. MacMillan Materials Research Laboratory Pennsylvania State University College Park, PA 16802	(1)	Dr. N. Tallan AFML Wright-Patterson AFB Dayton, OH 45433	(1)
Mr. F. Markarian Naval Weapons Center China Lake, CA 93555	(1)	Dr. T. Vasilos AVCO Corporation Research and Advanced Development Division 201 Lowell Street Wilmington, MA 01887	(1)
Dr. Perry A. Miles Raytheon Company Research Division 28 Sycamore Street Waltham, MA 02154	(1)	Mr. J.D. Walton Engineering Experiment Station Georgia Institute of Technology Atlanta, GA 30332	(1)
Mr. R. Rice Naval Research Laboratory Code 6360 Washington, D.C. 20375	(1)	Dr. S.M. Widerhorn Inorganic Materials Division National Bureau of Standards Washington, DC 20234	(1)

SUPPLEMENTARY DISTRIBUTION LIST (Cont'd)

<u>Organization</u>	<u>No. of Copies</u>
Dr. L.M. Gillin Aeronautical Research Laboratory P.O. Box 4331 Fisherman's Bend Melbourne, VIC 3001 AUSTRALIA	(1)
Dr. R. A. Tanzilli General Electric Company Reentry and Environmental Systems Division 3198 Chestnut Street Philadelphia, PA 19101	(1)
Professor John Field University of Cambridge New Cavendish Laboratory Cambridge, UNITED KINGDOM	(1)
Dr. B. R. Lawn Physics Department University of New South Wales Kingston, New South Wales AUSTRALIA	(1)

ATE
LMED
-8